

JGR Atmospheres

RESEARCH ARTICLE

10.1029/2018JD029387

Key Points:

- Extinction for dust with small amounts of iron was higher than for pure minerals but 19% to 21% lower than for background air particles
- Scattering decreased by <1% with increasing hematite mass in dust particles but decreased by 2% to 5% with increasing magnetite mass
- Dust backscatter fraction was 56% larger than for background air particles, SSA for dust with iron oxide or soot averaged 0.96 ± 0.06

Supporting Information:

- Supporting Information S1

Correspondence to:

J. M. Conny,
joseph.conny@nist.gov

Citation:

Conny, J. M., Willis, R. D., & Ortiz-Montalvo, D. L. (2019). Analysis and optical modeling of individual heterogeneous Asian dust particles collected at Mauna Loa Observatory. *Journal of Geophysical Research: Atmospheres*, 124. <https://doi.org/10.1029/2018JD029387>

Received 24 JUL 2018

Accepted 7 FEB 2019

Accepted article online 12 FEB 2019

Author Contributions:

Conceptualization: Joseph M. Conny**Formal analysis:** Joseph M. Conny, Robert D. Willis, Diana L. Ortiz-Montalvo**Methodology:** Joseph M. Conny**Supervision:** Joseph M. Conny**Writing - original draft:** Joseph M. Conny**Writing - review & editing:** Robert D. Willis, Diana L. Ortiz-Montalvo

Analysis and Optical Modeling of Individual Heterogeneous Asian Dust Particles Collected at Mauna Loa Observatory

Joseph M. Conny¹ , Robert D. Willis² , and Diana L. Ortiz-Montalvo¹ ¹Materials Measurement Science Division, National Institute of Standards and Technology, Gaithersburg, MD, USA,²Office of Research and Development, U.S. Environmental Protection Agency, Research Triangle Park, NC, USA (retired)

Abstract We have determined optical properties of heterogeneous particles from aerosol samples collected at Hawaii's Mauna Loa Observatory. Back trajectories, satellite imagery, and composition differences among particles from scanning electron microscopy revealed a subset of particles with dolomite or calcite that likely came from Asia. Using focused ion-beam tomography and the discrete dipole approximation, we show how small amounts of an iron phase (oxide or carbonate), or in one case soot, affected extinction and scattering compared with particles of neat dolomite or calcite. We show how particles exhibit a range scattering values due to varying orientations of the inclusion phases. Extinction efficiencies for the heterogeneous particles with dolomite (3.47) and calcite (3.36) were 19% to 21% lower than extinction for marine background air particles (3.72). Extinction for the Asian dust was, however, generally higher than for the neat particles. Compared to iron carbonate, the presence of an absorbing iron oxide affected scattering in Asian dust particles even at the low oxide concentrations studied here (0.6% to 8.1%). Scattering efficiency decreased by <1% with a 1% increase in hematite but by 2% to 5% with magnetite. Asian dust scattered light strongly forward, but backscattering was 56% larger than for the marine background air particles. Backscattering in the Asian dust was also larger with magnetite than hematite. Single scattering albedo for Asian dust with hematite, magnetite, or soot averaged 0.96 ± 0.06 ($\bar{x} \pm s$, $n = 19$) but was as low as 0.72 with a magnetite mass of 5.8%.

1. Introduction

The deserts of Asia are a large source of mineral dust injected into the atmosphere, second only to the Sahara (Tegen & Schepanski, 2009). While strong Asian dust storms are believed to have occurred periodically since before the common era (Chun et al., 2008), variation in the frequency of dust storms during the last century (Pye, 1987) is likely overall due more to climate change than desertification brought on by population growth and industrialization (X. Y. Zhang et al., 2003). Estimates of the amount of mineral dust injected into the atmosphere globally per year range from 1×10^{12} kg (1,000 Mt) to 4×10^{12} kg (4,000 Mt; Boucher et al., 2013). For Asian dust, primarily from the Gobi desert in Mongolia and the Taklimakan desert in northwest China, estimates of the amount injected per year vary widely from around 50×10^9 kg (50 Mt) for particles $<50 \mu\text{m}$ (Xuan et al., 2004) to 873×10^9 kg (873 Mt; Huang et al., 2014). Dust from the Taklimakan also redeposits within Asia such as in the downwind Loess region (Liu et al., 2011). In urban areas of China and South Asia, mineral dust accounts for an exceptionally large proportion, approximately 35%, of the mass for aerosols $<10 \mu\text{m}$ in size (Boucher et al., 2013).

Mineral dusts sampled in northwestern China and the Taklimakan region have shown aluminosilicate particles to be a substantial part of Asian dust (Okada & Kai, 1995; Okada & Kai, 2004). However, individual-particle analyses of balloon-platform samples at 3 to 5 km above the Taklimakan showed that 44% of the coarse particles ($>1.0 \mu\text{m}$ in diameter) had Ca as the dominant mass, comparable with Si (Iwasaka, 2003). In some samples from northwestern China (Okada & Kai, 1995), consistent mass ratios of Ca and Mg were believed to be due to dolomite. Calcium was also found to be internally mixed with aluminosilicates in coarse particles. Iwasaka and coworkers also showed that S was a component in about 35% of the coarse particles sampled.

If dust is lifted to the upper troposphere during a storm event, typically from February to May (Uematsu et al., 1983), strong midlatitude westerly winds can transport plumes thousands of kilometers across the Pacific to North America and beyond (Uno et al., 2009). Asian dust has been found in ice cores from

Published 2019. This article is a US Government work and is in the public domain in the USA.

Summit, Greenland, dating back 44,000 years (Svensson et al., 2000). Due to its location and longevity as an atmospheric research station, the Mauna Loa Observatory (MLO) in Hawaii has been a monitoring site for Asian dust since the 1970s (Bodhaine et al., 1981; Darzi & Winchester, 1982; Parrington et al., 1983; Shaw, 1980).

Early studies of the element composition of nonlocal dust at MLO showed high levels of Si, Fe, Al, K, and Ca compared to samples collected when Asian dust was believed to be minimal (Braaten & Cahill, 1986). Many elements including Fe and K (but not Al and Ca) were found to have higher concentrations than those found in Asian desert soils due to composition differences between the bulk soil and particles reaching MLO (Holmes & Zoller, 1996). High levels of S in Asian dust at MLO were suspected early on as a product of urban pollution from Asia (Darzi & Winchester, 1982). It appears that aluminosilicate dust, especially, absorbs SO₂ within the mainland, which further oxidizes, likely as (NH₄)₂SO₄ in marine air during flow eastward toward the Pacific Ocean (Formenti et al., 2011; Sullivan et al., 2007; Zhou et al., 1996).

Mineralogical studies have shown that individual dust particles often consist of multiple mineral components, such as quartz, feldspars, and clays (Fitzgerald et al., 2015; Jeong & Nousiainen, 2014; Shi et al., 2005). Jeong and Nousiainen (Jeong & Nousiainen, 2014) provided examples of how different minerals may be combined internally in Asian dust particles such as layers of clay minerals over a core of quartz, feldspar, calcite, and amphibole inclusions. Particles of nanofiber calcite interlaced with clay minerals and incorporated internally with quartz and feldspar have also been observed (Jeong & Chun, 2006).

As would be expected, dusts from different regions of the globe have distinct mineral signatures. For example, resuspended dust from northwestern China was found to have quartz, calcite, kaolinite, mica, and montmorillonite. In comparison, dusts from Morocco were found to have mainly quartz and illite and also plagioclase and orthoclase feldspars along with calcite, hornblende, and palygorskite (Engelbrecht et al., 2016). While clay minerals such as illite and smectites (e.g., montmorillonite) have been shown to be abundant from Asian dust samples taken across the Pacific (Leinen et al., 1994; Merrill et al., 1994) as well as in China (Jeong, 2008), the importance of calcium-containing minerals in Asian dust such as calcite and gypsum has also been reported (Engelbrecht et al., 2016; Fan et al., 1996; Jeong & Chun, 2006; Jeong & Nousiainen, 2014; Okada & Kai, 1995, 2004). Dust from the Loess Plateau downwind from the Gobi was found to have more Ca and less Si compared to Saharan dust. Calcium from both regions, though, is likely from carbonate minerals such as calcite and dolomite (Krueger et al., 2004). Dolomite has been detected in dust from the north margin of the Tibetan Plateau, and this region is believed to be a source of dolomitic dust during spring in Beijing (Li et al., 2007).

Radiative forcing by mineral dust particles, whether by direct cooling or warming of the atmosphere (direct effect), heating within the cloud layer (semidirect effect), or perturbing cloud microphysics via cloud condensation nuclei (indirect effect) is largely related to particle size and chemical composition (Hansen et al., 1997; Haywood & Boucher, 2000). Regional differences in the radiative forcing by dust are due to differences in mineral sources as well as climatic conditions for the release of dust at the surface (Huang et al., 2014). Compared to Saharan dusts, reports suggest that Asian dust is more absorptive, that is, exhibits a lower single scattering albedo (SSA, ratio of scattering to extinction), in the midregion of the solar spectrum (500 to 550 nm; Ge et al., 2010; Haywood et al., 2003; Lee et al., 2007).

While pollutants, such as soot or sulfate from SO₂ oxidation, adsorbed on particles may account in part for the lower SSA of Asian dust, the amount of free iron as an oxide, that is, iron that is not a structural part of a silicate, carbonate, or other nonabsorbing mineral phase (Sokolik & Toon, 1999), may also be a factor. The mass of free iron in Asian dust was, in fact, found to be higher (3.7%) than Saharan dust (2.8%; Lafon et al., 2004). Between goethite and hematite, the latter is typically more associated with Asian dusts (Lafon et al., 2006). When associated with clay minerals, discrete nanometer-sized iron oxide inclusions were observed within micrometer-sized clay soil particles (Greenland et al., 1968).

Optical properties of mineral dust particles are strongly affected by the internal mixing of free iron oxide because the imaginary part of the complex refractive index, which indicates absorption, is much larger for free iron oxides such as hematite than for iron-containing silicates and carbonates (Lafon et al., 2004, 2006). In addition to the effect on SSA, it has been suggested that solar backscattering varies inversely with the mass concentration of an absorbing iron oxide (Choobari et al., 2014; Flores et al., 1998).

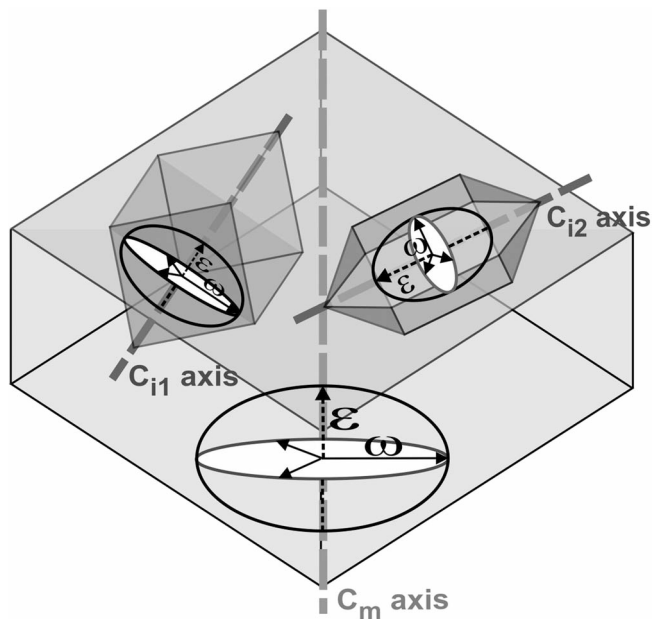


Figure 1. Simplified depiction of a heterogeneous particle containing two inclusions (dark gray phases) embedded within a matrix (light gray phase). The matrix and the inclusion on the left side represent uniaxial (–) phases such as dolomite and calcite. The indicatrices for these phases have refractive indices $\epsilon < \omega$. The inclusion on the right represents a uniaxial (+) phase such as quartz. The indicatrix for this phase has refractive indices $\epsilon > \omega$. Alignment of the optical axes of the inclusions (C_i axes) is different from the alignment of the matrix's optical axis (C_m axis) and represents variation in the spatial orientations of inclusions in the matrix.

In this work, we determined the composition and calculated optical properties of individual Asian dust particles collected at MLO along with particles from marine background air. The optical properties are derived from three-dimensional spatial models of each particle to depict its exact size, shape, and surface features. Particles were selected from the analysis of particle populations on filter samples by scanning electron microscopy (SEM) and energy dispersive X-ray spectroscopy (EDX). Using the discrete dipole approximation method for determining particle scattering (Draine & Flatau, 1994), optical properties were calculated from the 3-D spatial models of the particles, which were constructed from element maps by EDX and focused ion-beam (FIB) tomography associated with SEM as reported previously (Conny, 2013; Conny & Ortiz-Montalvo, 2017). We show how the absorbing phase, mainly iron-containing, in compositionally heterogeneous Asian dust at MLO affects particle optical behavior compared with size- and shape-equivalent homogeneous particles that lack an absorbing phase. In addition, we show how optical properties of heterogeneous Asian dust might vary depending on the spatial configuration of the phases.

The Asian dust particles selected for optical modeling in this study contained an iron phase. However, the question remained whether the iron phase was an absorbing oxide or a nonabsorbing iron-containing mineral. Therefore, we calculated the optical properties of the individually modeled particles to determine how an internally mixed iron-containing absorbing or nonabsorbing phase would affect extinction, scattering, SSA, and backscattering. As explained below, one particle was unusual in that it contained a soot adduct. In this case, the iron phase was determined to be a nonabsorbing aluminosilicate and the soot was the absorbing phase. To further determine the effect of composition heterogeneity, optical properties for the particles with all mineral phases included were compared with size- and shape-equivalent particles of a neat (pure) mineral phase.

In addition to employing FIB tomography to model optical properties, we considered how the variety of spatial arrangements of the mineral phases that exhibit optical anisotropy might affect the particle's optical properties. In anisotropic minerals, the vibration of an incident monochromatic light wave will change directions as it enters a crystal. When vibration of the light wave is aligned, either parallel or perpendicular, with the crystal's optical axis, then minerals with one optical axis (uniaxial) will have two refractive indices: a minimum and maximum. Minerals with two optical axes (biaxial) will have three refractive indices: a minimum, intermediate, and maximum. When the vibration of the light wave is not aligned with a crystal's optical axis, then the mineral will have intermediate refractive index values. Thus, how a heterogeneous particle behaves optically overall depends on how the optical axes of the individual phases within the particle are oriented with respect to incident light.

Figure 1 shows how three uniaxial phases, two inclusions (dark gray areas), and a matrix (light gray area) represented by different crystalline shapes, might be positioned in a heterogeneous particle. The three optical axes do not align. Included in Figure 1 are the uniaxial indicatrices for each phase. The indicatrices show the two refractive indices, ω (ordinary) and ϵ (extraordinary). The lengths of the vectors in each indicatrix represent the relative magnitudes of the refractive indices if vibration of the light wave were to align with the respective optical axes. If the phases are variously oriented within the particle, the particle would exhibit a range of refractive indices. In this study, the characteristic refractive indices for each mineral phase are used to calculate a lower and upper limit to the average refractive index for the particle using the Maxwell-Garnett dielectric function (e.g., Bohren & Wickramasinghe, 1977). The average refractive index is then used as input to the discrete dipole approximation method for calculating particle optical properties. The result is a range of possible values for the extinction, scattering, and the backscatter fraction for each particle.

2. Methods

2.1. Sampling at MLO

MLO (19° 32′ 10″N, 155° 34′ 34″W) is located on the north slope of the Mauna Loa volcano, approximately 5 km from the summit, on the island of Hawaii within the Hawaiian archipelago. The observatory's elevation is 3.397 km. Upslope flow to Mauna Loa during daytime typically brings some locally emitted aerosol to MLO. Downslope flow at night typically brings aerosols from remote sources (Mendonca, 1969). Twelve samples with particles up to 10 μm in size (PM_{10}) were collected on polycarbonate membrane (Nuclepore) filters at MLO during 15 March to 26 April 2011. The sampler was a Versatile Air Pollutant Sampler virtual impactor (URG Corporation) operating at 32 L/min. (Commercial products identified here specify the means by which experiments were conducted. Such identification is intended neither to imply recommendation or endorsement by the National Institute of Standards and Technology nor imply that the identified products are necessarily the best available for the purpose.) Six samples were collected during daytime hours, 6 a.m. to 6 p.m. (“D” samples), and six were collected during nighttime hours, 6 p.m. to 6 a.m. (“N” samples). Collection was integrated for 72 hr. Daytime and nighttime field blanks were collected by installing the filters in the sampler and then immediately removing them without having active air flow through the sampler. Dust samples from the vicinity of the Observatory were taken from the lava field, road, and parking lot. At each location, three bulk samples were collected using a clean scoop, stored in zip-lock bags, and later composited. The composited samples were then sieved through a fine-mesh screen to remove large particles. Remaining small particles were then deposited on the polycarbonate filters. Table S1 in the supporting information lists the samples and collection dates.

On 19–20 March 2011 and again on 21 March 2011, the Korean Meteorological Administration recorded elevated levels of PM_{10} (400 to 876 $\mu\text{g}/\text{m}^3$) at many monitoring stations on the Korean Peninsula (Korean Meteorological Administration, 2011). On other days between 5 March and 26 April $<100\text{-}\mu\text{g}/\text{m}^3$ dust was observed over the Korean Peninsula, far lower than the 19–21 March dust events.

Back trajectories with HYSPLIT. (Draxler, 1999; Giles et al., 2006; Stein et al., 2015) in Figure 2 show that high-concentration dust plumes likely reached the Hawaiian Islands around 24–25 March. Meteorological wind roses (Figure S1 in the supporting information) show that prevailing winds were from the east for the majority of samples. In Figure 2, the HYSPLIT. back trajectories from Asia show air circling from the north and approaching MLO from the east at an altitude of between 2 and 5 km. Air masses at 3 and 5 km likely originated from eastern China 7 days prior. At the 3.4-km elevation of MLO, the Asian dust plume recorded 4 to 6 days prior on the Korean Peninsula was likely captured at MLO by one or more of the 1D to 4N samples.

Global aerosol maps from the Navy Aerosol Analysis and Prediction System (<https://www.nrlmry.navy.mil/aerosol/>; Christensen, 1997; Hogan & Brody, 1993; Hogan & Rosmond, 1991; Figure S2 in the supporting information) for 19, 21, 24, and 25 March 2011 show dust originating from the Asian mainland, traveling over the Korean Peninsula and reaching the Hawaiian Islands around 24 March. Figure S2 also shows that dust along with smoke likely reached the Hawaiian Islands on 19 and 20 March 2011. In addition, elevated dust levels were recorded at three U.S. Environmental Protection Agency monitoring sites on Oahu on 24 March 2011 (Figure S3 in the supporting information). Thus, the dust event on the Korean Peninsula, back trajectories, global aerosol maps, and dust monitoring on Oahu suggests that samples 3D and 4N were collected when Asian dust likely reached MLO. Samples 1D and 2N may also have been impacted by Asian dust.

2.2. Particle Population Analysis and Classification

Analysis of particle populations for element composition and particle morphology from 18 samples (Table S1 in the supporting information) was performed with a Tescan MIRA3 scanning electron microscope (Tescan USA, Inc.) equipped with a PulseTor EDX detector in automated analysis mode, that is, as computer-controlled SEM. The electron beam energy and current were 20 kV and 0.55 nA, respectively. A $5 \times 5\text{-mm}$ section of each filter sample was coated with 20 nm of carbon to prevent charging of the substrate by the electron beam. The backscattered electron signal was used to locate particles on the substrate. EDX analysis was conducted for 1.5 s on each particle to yield concentrations for 20 elements for the purpose of particle classification. For the 12 atmospheric samples, two size ranges were analyzed: 0.4 to 1.5 μm and 1.5 to 10 μm . For

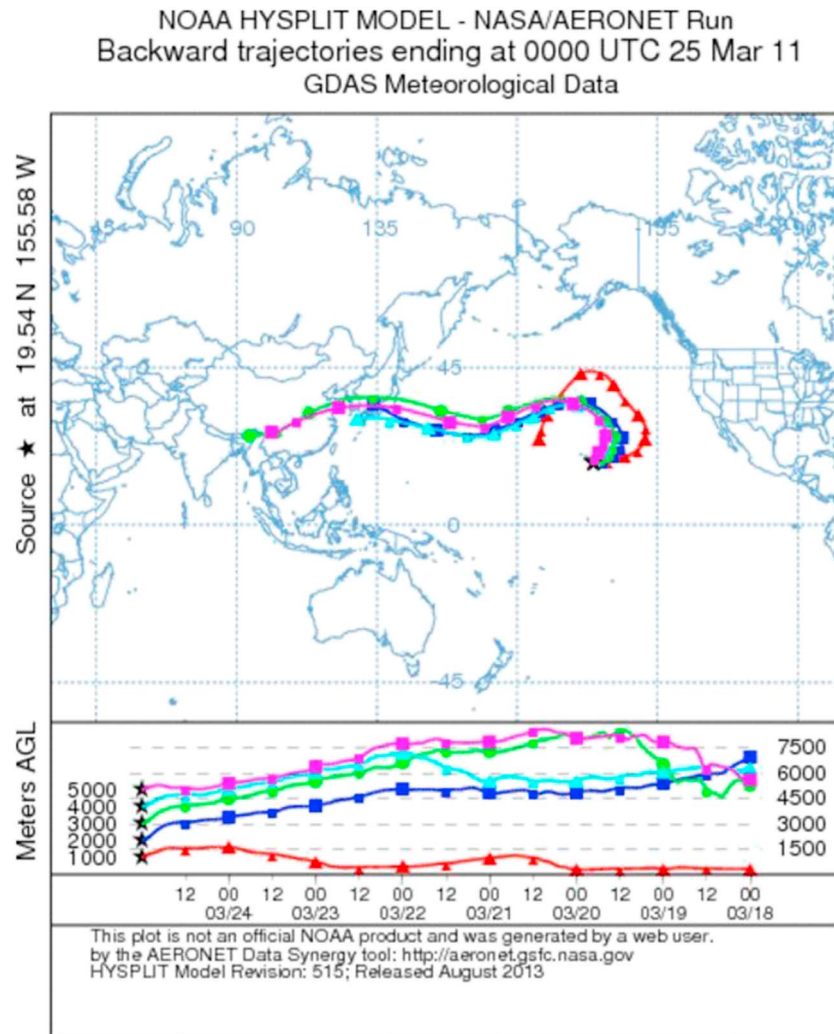


Figure 2. HYSPLIT back trajectories starting on 25 March 2011 and ending on 18 March 2011. Four air masses are shown reaching MLO from Asia at altitudes of 2 to 5 km. The elevation of MLO is 3.4 km. MLO = Mauna Loa Observatory; NOAA = National Oceanic and Atmospheric Administration; NASA = National Aeronautics and Space Administration; AERONET = AErosol RObotics NETwork; GDAS = Global Data Assimilation System.

samples taken from the lava field, road, and parking lot, only particles 1.5 to 10 μm were analyzed. In each size range, 800 particles were analyzed. Using the classification rules involving elements as shown in Table 1, particles were initially placed in 21 classes. Similar classes were then combined to form 12 condensed particle classes.

2.3. Individual Particle Analysis and Focused Ion-Beam Tomography

Individual particles identified as Asian dust or marine background aerosol based on the particle population analysis and classification were selected for further analysis by EDX element mapping with a FIB-SEM instrument (FEI Nova NanoLab 600 DualBeam, Thermo-Fisher Scientific). Imaging and element analysis of the particles was performed with the electron beam in raster mode at 20 kV and 0.62 nA. While operating as a scanning electron microscope, the FIB-SEM instrument may also be used to mill specimens with a gallium ion beam. In FIB tomography, the particle specimen is sequentially sliced while SEM images are collected. The resulting series of images (typically numbering 100 to 200) is then used to create a three-dimensional spatial model of the particle using Avizo version 7 3-D visualization and modeling software

Table 1
Classification Scheme for Particles from Atmospheric Samples, Ground Samples from the Vicinity of MLO, and Blanks

Final class	Initial class	Classification rules ^a	Rule order ^b
quartz	quartz	Si > =75%	2
S + Si	S + Si	S > =25% and Si > 27% and [Al/Si] < 0.15	5
Ca-S	Ca-S	[Ca + S] > 60 and S > 0% and [Ca/S] < 2.5 and [Ca/S] > 0.4	8
Fe rich	Fe	Fe > 70%	6
	Fe rich	first_element = Fe and Fe > =40%	20
Na-S	Na-S (1)	S > Mg and S > Al and S > Si and S > Ca and S > Fe and S > K and S > Ti and [Ca/S] < 0.4 and Na > Mg and Na > Al and Na > Si and Na > Fe and S > Ti	9
	Na-S (2)	[Na + S] > 50% and Na > 20% and S > 20%	13
	S	S > 80%	7
Na-Al-Si	Na-Al-Si	[Na + Al + Si] > 50% and [Al + Si] > 50% and Na > =11%	11
Al-Si	Al-Si	[Al + Si] > =74% and Si > 0% and [Al/Si] > 0.15	12
	mixed Al-Si	[Al + Si] > 40%	18
	(Al-Si) + (Ca-S)	[Al + Si] > =27% and [Ca + S] > =25% and S > 0% and [Ca/S] > 0.5 and [Ca/S] < 1.5	3
	S+(Al-Si)	S > =25% and Si > 10% and [Al + Si] > 20% and [Al/Si] > =0.15	4
Mg-Al-Si	Mg-Al-Si	[Mg + Al + Si] > 50% and Mg < [Al + Si] and [Al + Si] > 50% and Mg > =8%	14
Ca rich	Ca	Ca > 87%	15
	Ca rich (1)	first_element = Ca and Ca > =40%	17
	Ca rich (2)	Ca > 50%	19
Mg-Ca	Mg-Ca	[Mg + Ca] > 60% and Mg > 25% and Ca > 25%	16
Ti rich	Ti rich	first_element = Ti	21
miscellaneous	Metal rich	video ^c > 115 and [Cr > 5% or Mn > 5% or Ni > 5% or Cu > 5% or Zn > 5% or Pb > 5%]	1
	Carbon sulfate	counts ^d < 300 and video ^c < 100	10
	Remainder	true	22

Note. MLO = Mauna Loa Observatory.

^aCommand syntax used with software installed on Tescan MIRA3 microscope. ^bOrder that initial classification rules were run such that particles were “sieved” through rules 1 to 22. ^cBackscattered electron intensity. ^dX-ray photon counts.

(Thermo-Fisher Scientific). Details about FIB tomography of atmospheric particles were reported previously (Conny et al., 2014; Conny & Ortiz-Montalvo, 2017).

2.4. Optical Property Modeling

We used DDSCAT version 7.3 (Draine & Flatau, 1994, 2013) to implement the discrete dipole approximation method for calculating extinction and scattering efficiencies, SSA, and the backscatter fraction of selected particles at 589-nm incident light. Efficiencies are the optical cross sections of a particle divided by the cross-sectional area of a volume-equivalent sphere. In DDSCAT, a particle is defined as a target within a lab (computational) frame of reference. To simulate the random orientation of the particle within the atmosphere, the target is rotated within the lab frame. Rotation is defined by three angles, Θ , Φ , and β . Angles Θ and Φ specify the position of the target in the lab frame relative to the direction of incident light. The β specifies the rotation of the target about its axis. In the lab frame, the target was positioned at intervals such that Φ increased from 0° to 360° in increments of 60°. Θ increased in steps at 0°, 60°, 90°, 120°, and 180°, that is, in uniform intervals of $\cos(\Theta)$ from 1 to -1. The target was rotated about its axis such that β was incremented by 60° from 0° to 360°. See Draine and Flatau (2013) for a graphical explanation of Θ , Φ , and β in the lab frame.

Scattering directions in DDSCAT are defined by two angles φ and θ . Phi positions the scattering planes within the lab frame. Theta specifies the scattering direction at each plane. Four scattering planes were positioned at $\varphi = 0^\circ, 90^\circ, 180^\circ, \text{ and } 270^\circ$. Scattering at each plane was calculated for θ from 0° to 180° in 5° intervals.

All particles in this study contained multiple mineral phases. As mentioned in section 1, we accounted for the optical behavior of the various mineral phases by determining an average complex refractive index with the Maxwell-Garnett dielectric function, whereby a phase of small mass is considered as an inclusion within a different phase of larger mass (matrix). As shown previously (Conny & Ortiz-Montalvo, 2017), we

determined the average Maxwell-Garnett dielectric function by adding an inclusion phase to the matrix sequentially.

$$\begin{aligned} \epsilon_{1,2} &= \epsilon_1 \left[1 + \frac{3f_2 \left(\frac{\epsilon_2 - \epsilon_1}{\epsilon_2 + 2\epsilon_1} \right)}{1 - f_2 \left(\frac{\epsilon_2 - \epsilon_1}{\epsilon_2 + 2\epsilon_1} \right)} \right] \rightarrow \epsilon_{1,2,3} = \epsilon_{1,2} \left[1 + \frac{3f_3 \left(\frac{\epsilon_3 - \epsilon_{1,2}}{\epsilon_3 + 2\epsilon_{1,2}} \right)}{1 - f_3 \left(\frac{\epsilon_3 - \epsilon_{1,2}}{\epsilon_3 + 2\epsilon_{1,2}} \right)} \right] \rightarrow \dots \rightarrow \epsilon_{1,2,3,\dots,n} \\ &= \epsilon_{1,2,3,\dots,(n-1)} \left[1 + \frac{3f_n \left(\frac{\epsilon_n - \epsilon_{1,2,3,\dots,(n-1)}}{\epsilon_n + 2\epsilon_{1,2,3,\dots,(n-1)}} \right)}{1 - f_n \left(\frac{\epsilon_n - \epsilon_{1,2,3,\dots,(n-1)}}{\epsilon_n + 2\epsilon_{1,2,3,\dots,(n-1)}} \right)} \right] \end{aligned} \quad (1)$$

Here, $\epsilon_{1,2}$, $\epsilon_{1,2,3}$, and $\epsilon_{1,2,3,\dots,n}$ are Maxwell-Garnett average dielectric functions that combine an inclusion phase with the matrix at the first, second, and last steps in the sequence. ϵ_1 , ϵ_2 , ϵ_3 , and ϵ_n , are the dielectric functions for the largest, second largest, third largest, and smallest volume minerals in the particles, respectively. The f_2 , f_3 , and f_n , are the volume fractions for the second, third, and smallest inclusion phases. In the first equation above representing the first step in the sequence, $\epsilon_{1,2}$ is the average dielectric function for the largest mineral as the matrix and the second largest mineral as the inclusion phase. In the second equation above representing the second step, $\epsilon_{1,2,3}$ is the average dielectric function combining the result of the first sequence step, $\epsilon_{1,2}$, as the matrix and the third largest mineral as the inclusion phase. In the third equation above representing the final step, $\epsilon_{1,2,3,\dots,n}$ is the final average dielectric function combining the second to last sequence step, $\epsilon_{1,2,3,\dots,(n-1)}$, as the matrix and the smallest mineral as the inclusion phase. The average dielectric function for the particle is related to real (n) and imaginary (k) parts of the complex refractive index as follows (Bohren & Huffman, 1983):

$$n = \left[\frac{\sqrt{\epsilon''^2 + \epsilon'^2} + \epsilon'}{2} \right]^{1/2} \quad (2)$$

$$k = \left[\frac{\sqrt{\epsilon''^2 + \epsilon'^2} - \epsilon'}{2} \right]^{1/2} \quad (3)$$

If we assume that mineral phases within a particle are crystalline, then depending on the crystal structure, the particle is likely optically anisotropic with multiple refractive indices. To determine minimum and maximum limits to the complex refractive index for a particle, we considered minimum and maximum values for the real part of the refractive index for the individual mineral phases. Uniaxially anisotropic minerals have two principal refractive indices for the real part, ω (ordinary) and ϵ (extraordinary), while biaxially anisotropic minerals have three principal refractive indices, α , β , and γ . For biaxial minerals, α is the smaller refractive index and γ the larger. For uniaxial positive minerals, ω is the larger refractive index; for uniaxial negative minerals ϵ is the larger refractive index (Bloss, 1961). In determining a particle's minimum complex refractive index from equations (1)–(3), the minimum value for the complex dielectric function of individual minerals was based on the smaller real refractive index. Likewise, the maximum complex refractive index was based on the larger real refractive index.

For the backscatter fraction, we calculated the fraction of light intensity scattered from 90° to 180° rather than directly backward, that is, at 180° , as is often done. The differential scattered light intensity is calculated from the differential scattering cross section (Draine & Flatau, 2013) as follows:

$$\frac{dC_{\text{sca}}}{d\Omega} = \frac{1}{k^2} S_{11} \quad (4)$$

Here, C_{sca} is the scattering cross section at the solid angle Ω , $k = 2\pi/\lambda$ where λ is the wavelength of light ($0.589 \mu\text{m}$), and S_{11} is the first Mueller matrix element. The backscatter fraction is the ratio of the integral from 90° to 180° to the integral from 0° to 180° :

Table 2
Percent Mass Concentrations of Major Elements, Excluding Carbon and Oxygen, From Particle Population Analyses

Sample	Na	Mg	Al	Si	S	K	Ca	Fe
1D	3.00	6.29	21.91	42.73	5.71	3.76	12.54	3.34
2N	2.58	6.63	22.12	42.49	4.44	3.55	14.11	3.28
3D	2.05	5.44	22.47	45.35	3.45	3.84	13.50	3.06
4N	1.93	5.26	21.89	45.72	3.60	3.84	13.78	3.41
5D	5.89	3.38	19.57	38.20	16.17	3.56	9.48	2.79
5D duplicate	5.57	3.21	20.12	41.60	14.21	3.36	7.82	3.12
6N	3.15	3.20	21.15	43.83	11.45	3.92	9.48	3.29
6N duplicate	2.57	3.13	21.50	44.33	11.04	4.03	9.54	3.18
7D	4.34	0.53	15.85	47.34	23.16	2.09	5.07	1.07
8N	3.60	3.59	17.28	40.88	22.75	2.55	5.92	2.75
9D	4.22	0.53	15.96	48.86	21.95	2.15	4.95	0.89
10N	4.05	0.85	13.87	39.69	32.62	1.23	6.48	0.75
11D	11.48	2.22	9.66	26.57	44.26	1.31	3.33	0.64
12N	10.70	1.91	11.95	32.20	36.86	1.78	3.11	1.10
$\bar{x} \pm s$	4.6 ± 2.7	3.3 ± 1.8	18.5 ± 3.9	41.5 ± 5.4	17.4 ± 11.8	3.0 ± 1.0	8.6 ± 3.5	2.4 ± 1.1
Parking lot	2.62	4.03	29.51	44.11	0.02	0.66	6.02	11.22
Road field	2.87	5.31	22.23	51.87	0.55	0.54	10.16	5.14
Lava field	2.91	5.53	22.02	51.83	0.73	0.56	10.13	5.03

$$\int_{90}^{180} S_{11} d\Omega / \int_0^{180} S_{11} d\Omega = \sum_{90}^{180} S_{11} \Delta\Omega / \sum_0^{180} S_{11} \Delta\Omega \quad (5)$$

From (Draine & Flatau, 2013), $\Delta\Omega$ is determined as follows:

$$\Omega_{j,k} = \frac{\pi}{N_{\varphi}(j)} [\cos(\theta_{j-1}) - \cos(\theta_{j+1})], \quad j = 2, \dots, N_{\theta}-1 \quad (6)$$

$$\Omega_{1,k} = \frac{2\pi}{N_{\varphi}(1)} \left[1 - \frac{\cos(\theta_1) + \cos(\theta_2)}{2} \right] \quad (7)$$

$$\Omega_{N_{\varphi},k} = \frac{2\pi}{N_{\varphi}(N_{\theta})} \left[\frac{\cos(\theta_{N_{\theta}-1}) + \cos(\theta_{N_{\theta}})}{2} + 1 \right] \quad (8)$$

Here, θ and φ are the scattering angles described above. N_{φ} is the number of scattering planes with angles φ . N_{θ} is the number of θ angles within a scattering plane. $\theta = \theta_j, j = 1, \dots, N_{\theta}$. $\varphi = \varphi_{j,k}, k = 1, \dots, N_{\varphi}$.

3. Results and Discussion

3.1. Analysis of Particle Populations

For the 12 daytime and nighttime atmospheric samples, the number of particles per square millimeter of filter area (which is proportional to the concentration of like-sized particles in air) ranged from 1,523 (sample 9D) to 13,082 (sample 4N). Field and lab blanks, for which sampling duration was negligible, had particle loadings 2 to 4 orders of magnitude lower. Table 2 shows the percent mass concentration of the major elements in the 1.5- to 10- μm particle size range for the 12 atmospheric samples along with the three samples from the vicinity of the observatory. Carbon and oxygen were excluded in the particle population analysis due to the polycarbonate filter material. Si, Al, and S contributed the most to the particle mass on average for the atmospheric samples. The lava field, road, and parking lot samples also had high Si and Al but far lower S than the atmospheric samples. The variation in S mass for the atmospheric samples in Table 2 is more than twice that for other elements. Sulfur is also markedly low in samples 1D-4N.

Figure 3 shows the percent of particles in each sample that were assigned to the 12 particle classes. For the atmospheric samples (1D to 12N), the two particle size groups are combined so that particle sizes range from 0.4 to 10 μm . For the lava field, road, and parking lot samples, only particle sizes 1.5 to 10 μm are shown.

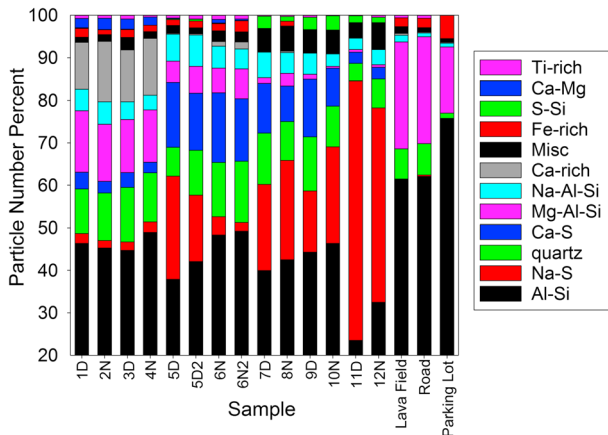


Figure 3. Percent of particles among the 12 particle classes for the atmospheric samples (1D to 12N) and bulk dust samples collected in the vicinity of Mauna Loa Observatory (lava field, road, and parking lot). Particle sizes for the atmospheric samples are 0.4 to 10 μm . Particle sizes for the lava field, road, and parking lot samples are 1.5 to 10 μm . Repeated colors in the chart follow the color positions in the legend. For example, the Na-S class (red) is toward the bottom of the chart and the Fe-rich class (red) is toward the top of the chart.

Among all samples, a large percentage of the particles are in the Al-Si class. The atmospheric particles exhibit a larger variety of compositions than the samples from the grounds. Particles from the grounds mainly belong to two classes: Al-Si and Mg-Al-Si.

Figure 3 also shows that the aerosol chemistry changed during the sampling interval. Within the first samples, 1D-4N, there are substantially fewer Ca-S particles compared to the later samples (5D-10N). In contrast, there are substantially more Ca-rich particles among samples 1D-4N compared to later atmospheric samples. Similarly, more Mg-Al-Si particles appear to be in samples 1D-4N than in later samples. However, the lava field, road, and parking lot samples also contain large numbers of Mg-Al-Si particles, so the Mg-Al-Si class cannot be used reliably to distinguish samples 1D-4N from later atmospheric samples. Ca-S and Ca-rich particles are not observed in the lava field, road, and parking lot samples.

There are relatively few Ca-Mg particles in the samples overall, but as Figure 4 shows, the relative distribution of Ca-Mg particles among samples is similar to that for the Ca-rich particles. Figure 4 reveals that the calcium-containing Ca-rich and Ca-Mg particles best represent samples 1D-4N while sulfur-containing Ca-S and, to a lesser extent, Na-S particles represent samples taken later in the sampling interval.

It is likely that Asian dust was collected in samples 3D and 4N between 22 and 28 March 2011 based on multiple lines of evidence: (1) meteorological back trajectories from Hawaii to the recorded dust events on the Korean Peninsula (Figure 2), (2) Navy Aerosol Analysis and Prediction System map sequence showing dust movement from the Korean Peninsula to Hawaii (Figure S2 in the supporting information), and (3) elevated dust events recorded at multiple sites on Oahu on 24 March 2011 (Figure S3 in the supporting information). Since samples 1D-4N are distinguished by the presence of Ca-rich and Ca-Mg particles, we surmise that the Ca-rich and Ca-Mg particles in samples 3D and 4N are Asian dust. Moreover, since Figure 4 shows that the percentages of Ca-rich particles in 1D versus 3D and in 2N versus 4N are nearly identical, it is likely that Ca-rich particles in 1D and 2N are also Asian dust. By the same argument, the Ca-Mg particles in 1D and 2N are probably also Asian dust. The presence of few Ca-S particles in 1D-4N, as well as in the lava field, road, and parking lot samples (Figure 3), suggests that Ca-S particles are not associated with Asian dust but rather with marine background air.

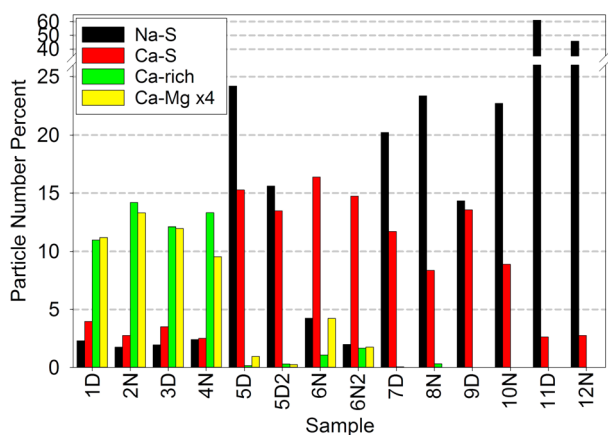


Figure 4. Percent of particles in four classes that distinguish samples 1D to 4N from later samples. Note that Ca-Mg particles in samples 1D to 4N are a small fraction (1.9% to 2.7%) of the total number of particles in each sample. Particle sizes are 0.4 to 10 μm .

3.2. Element Compositions of Individual Particles

Individual Ca-Mg, Ca-rich, and Ca-S particles were selected from the four samples that likely contained Asian dust (1D-4N). Among the Asian dust particles, we selected one Ca-Mg particle and one Ca-rich particle from each of samples 1D, 2N, and 3D. Since sample 4N was likely impacted more by Asian dust than other samples, we selected two Ca-Mg and two Ca-rich particles (labeled as 4N1 and 4N2) for a total of five each of the Ca-Mg and Ca-rich particles. For the Ca-S particles associated with marine background air, we selected one particle from each of the four samples. In determining element concentrations from element mapping by EDX, oxygen composition was determined stoichiometrically and all measured elements were assumed to exist in the oxidized state.

3.2.1. Ca-Mg Particle Maps

Figures 5a–5e show secondary electron images, element maps, and the element compositions (excluding carbon) of the five selected Ca-Mg particles. Ca and Mg are the most abundant elements followed for the most part by Si and Al or Si and S. The predominance of Ca and Mg with comparable atomic percent amounts suggests that the particles contain a dolomite phase ($\text{CaMg}(\text{CO}_3)_2$). Thus, dolomite was assigned as the major

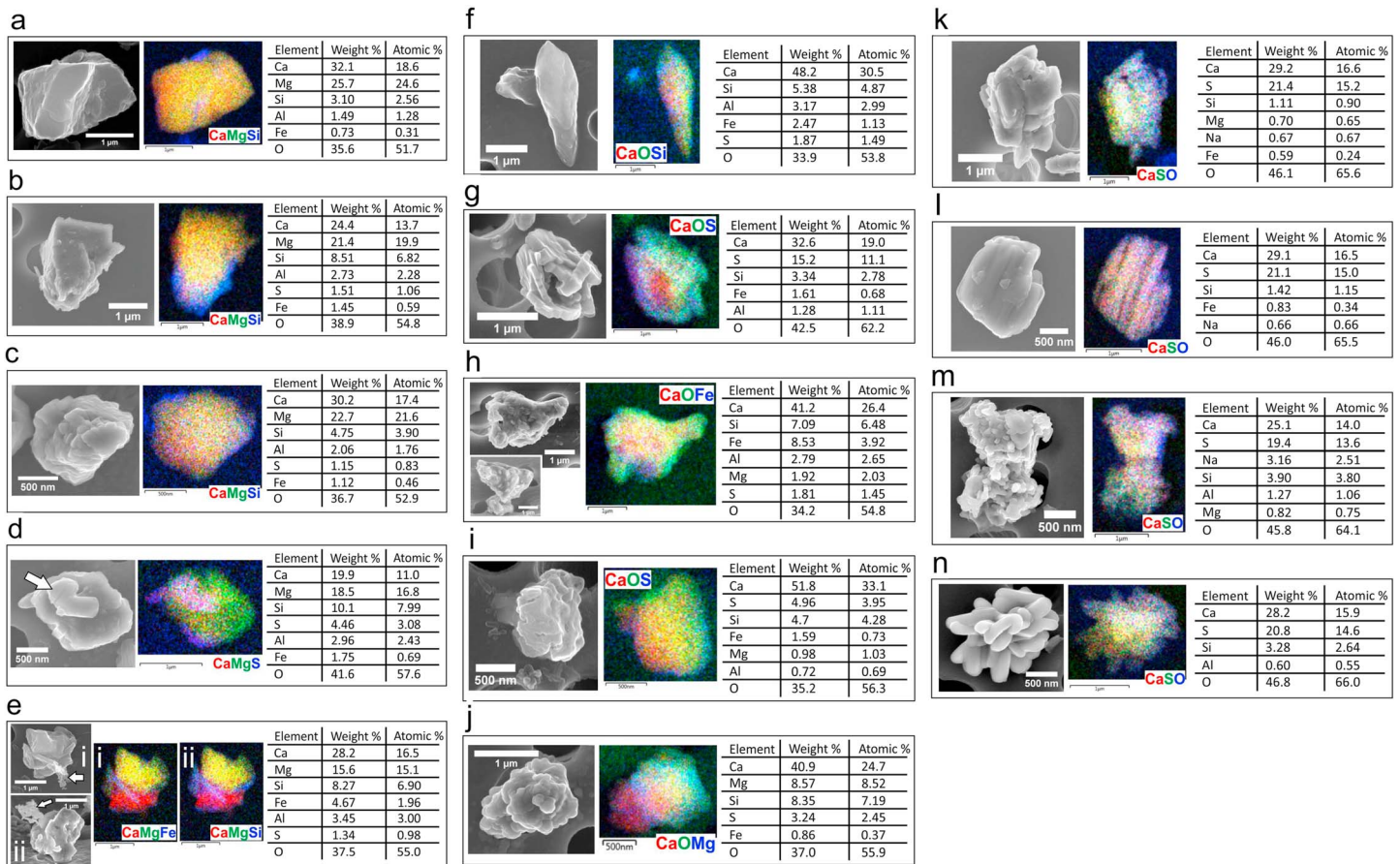


Figure 5. Secondary electron images, element maps, and element compositions of Ca-Mg, Ca-rich, and Ca-S particles. (a–e) Ca-Mg particles 1D, 2N, 3D, 4N1, and 4N2. (f–j) Ca-rich particles 1D, 2N, 3D, 4N1, and 4N2. (k–n) Ca-S particles 1D, 2N, 3D, and 4N. Particle Ca-Mg 4N1 (d) has a sulfate adduct (arrow). Particle Ca-Mg 4N2 (e) has a soot adduct (arrows). In (e) secondary electron image (i) is with electron beam at normal. Secondary electron image (ii) is with the stage tilted such that the electron beam is at 60° from normal. Both element maps in panel (e) are taken with the electron beam at normal. Carbon was not included in the energy dispersive X-ray spectroscopy analysis. Oxygen was determined stoichiometrically. RGB colors are additive; for example, red + green = yellow, and red + green + blue = white.

phase. As Figure 5 shows, Fe is also present in all Ca-Mg particles. Iron can replace Mg in dolomite, and as a result, ankerite ($\text{CaFe}(\text{CO}_3)_2$) often exists in solid solution with dolomite (Deer et al., 2013).

The Ca-Mg particles from samples 1D–3N (Figures 5a–5c) show little spatial variation in the element maps that can be attributed to structural features of the particles. However, the two 4N particles (Figures 5d and 5e) do show compositional and structural variation. In Figure 5d, the particle has a surface inclusion (see arrow) that contains S with Ca, suggesting a gypsum adduct.

The second 4N particle (4N2; Figure 5e) shows multiple spatial features. First, the presence of an iron silicate phase in the element maps (i and ii) is a distinctive feature in the electron image. Second, the element maps show a phase containing Ca in the lower part of the particle that is separate from the dolomite phase in the upper part of the particle. The phase is assumed to be calcite (CaCO_3). Finally, a soot-like carbon phase (see arrows in figure) that is easily identified from its morphology is in the electron image viewed at normal (image i) and at 60° from normal (image ii).

3.2.2. Ca-Rich Particle Maps

Element compositions along with secondary electron images and element maps for the five selected Ca-rich particles are shown in Figures 5f–5j. As with the Ca-Mg particles, carbon was not measured and oxygen was determined stoichiometrically. Except for particle 2N (Figure 5g), Ca in these particles was at least 5 times more abundant by mass than other elements. Calcite in Asian dust has been widely reported (Cao et al., 2005; Jeong, 2008; Jeong & Chun, 2006; Okada & Kai, 1995); thus, we assign calcite as the predominant

Table 3
Mass and Volume Percent of Mineral Phases in Ca-Mg Asian Dust Particles

Particle	Mineral phase	Mass percent	Volume percent	Mass percent	Volume percent	Mass percent	Volume percent
		With ankerite		With hematite		With magnetite	
1D Ca-Mg	Dolomite	79.4	78.9	81.0	80.5	81.0	80.5
	Magnesite	12.4	11.8	11.9	11.3	11.9	11.2
	Montmorillonite	5.69	6.47	5.71	6.49	5.70	6.49
	Ammonium sulfate	0.89	1.43	0.90	1.44	0.90	1.44
	Iron containing	1.54	1.41	0.58	0.31	0.55	0.30
2N Ca-Mg	Dolomite	63.6	61.5	66.8	64.7	66.8	64.7
	Montmorillonite	14.5	16.1	14.6	16.2	14.6	16.2
	Magnesite	14.9	13.7	13.7	12.6	13.7	12.6
	Ammonium sulfate	3.69	5.77	3.70	5.81	3.70	5.80
	Iron containing	3.32	2.96	1.23	0.65	1.19	0.64
3D Ca-Mg	Dolomite	76.4	74.7	78.8	77.1	78.8	77.1
	Montmorillonite	8.90	9.95	8.94	10.0	8.94	10.0
	Magnesite	9.61	8.96	8.70	8.12	8.71	8.13
	Ammonium sulfate	2.67	4.22	2.68	4.25	2.68	4.24
	Iron containing	2.44	2.20	0.90	0.48	0.87	0.47
4N1 Ca-Mg	Dolomite	38.7	36.9	42.7	40.9	42.7	40.9
	Magnesite	23.5	21.4	22.0	20.1	22.0	20.0
	Montmorillonite	18.0	19.7	18.2	19.9	18.2	19.9
	Gypsum	15.4	18.2	15.5	18.3	15.5	18.3
	Iron containing	4.35	3.83	1.62	0.84	1.56	0.83
4N2 Ca-Mg ^a		With annite					
	Dolomite	59.7	60.0				
	Montmorillonite	10.6	12.1				
	Calcite	9.56	10.1				
	Annite	8.50	7.36				
	Magnesite	5.00	4.77				
	Ammonium sulfate (Soot)	3.29 3.48	4.06 1.96				

^aVolume of soot is determined from focused ion-beam tomography. Mass of soot is based on an assumed density of 1.77 g/cm³ (Park et al., 2004).

phase. Particle 2N is relatively high in S as well as Ca; however, the particle was classified by computer-controlled SEM as Ca rich (Table 2). Magnesium, Al, Si, S, and Fe were also detected in all Ca-rich particles. (Some elements detected but with concentrations close to or less than 1% are not shown in Figure 5.) Since Fe²⁺ may substitute for Ca²⁺, siderite (FeCO₃) may coexist with CaCO₃ (Deer et al., 2013).

3.2.3. Ca-S Particle Maps

The four selected particles associated with marine background air are shown in Figures 5k–5n. As with other particles, Ca is most abundant, however, S is a close second. Other elements including Al, Mg, Fe (not all shown in Figure 5), and Si are present but at much lower levels. The nearly equal atomic abundances of Ca and S in Figures 5k–5n suggest that the particles are primarily gypsum (CaSO₄·2H₂O). Thus, gypsum was assigned as the predominant phase.

3.3. Phase Volumes in Individual Particles

Volumes of individual phases in the particles were determined stoichiometrically by first assigning oxygen to the carbonate anion in the Asian dust particles or to the sulfate anion in the marine background air particles. Remaining phases in the Asian dust and marine background air particles were assigned and apportioned stoichiometrically as described below. Mineral densities were then used to calculate the percent volume of each phase.

As mentioned earlier, all Asian dust particles in this study had a measurable amount of Fe. With one exception (Ca-Mg 4N2), the Asian dust particles did not exhibit a distinct Fe phase in the element map that could be associated with another element such as Si or with a structural feature on the particle. Therefore, the Fe phase was determined both as a nonabsorbing phase, such as an iron carbonate (e.g., ankerite), or as an absorbing iron oxide, in this case hematite or magnetite. While hematite is the iron oxide most associated

Table 4
Mass and Volume Percent of Mineral Phases in Ca-rich Asian Dust Particles

Particle	Mineral phase	Mass percent	Volume percent	Mass percent	Volume percent	Mass percent	Volume percent
		With siderite		With hematite		With magnetite	
1D Ca-rich	Calcite	74.7	74.9	75.4	74.4	75.5	74.4
	Albite/anorthite/orthoclase	13.6	13.9	13.7	13.8	13.7	13.8
	Ammonium sulfate	4.80	5.63	4.84	7.32	4.85	7.32
	Magnesite	3.78	3.42	3.82	3.40	3.82	3.40
	Iron containing	3.18	2.19	2.22	1.13	2.15	1.11
2N Ca-rich	Gypsum	60.8	64.9	61.3	65.4	61.3	65.4
	Calcite	25.1	22.9	25.3	23.1	25.3	23.1
	Albite/anorthite/orthoclase	9.71	9.04	9.78	9.11	9.78	9.10
	Magnesite	1.87	1.54	1.88	1.55	1.88	1.55
	Iron-containing	2.48	1.55	1.73	0.81	1.67	0.80
3D Ca-rich	Calcite	62.6	64.4	64.9	67.0	65.1	67.0
	Albite/anorthite/orthoclase	14.9	15.7	15.5	16.3	15.5	16.3
	Iron containing	11.4	8.03	8.14	4.33	7.90	4.26
	Gypsum	6.26	7.53	6.50	7.84	6.50	7.83
	Magnesite	4.28	3.98	4.45	4.15	4.28	3.98
	Rhodochrosite	0.50	0.38	0.52	0.40	0.50	0.38
4N1 Ca-rich	Calcite	72.3	70.8	72.8	71.3	72.8	71.3
	Gypsum	17.1	19.6	17.2	19.7	17.2	19.7
	Quartz/anorthite	6.30	6.27	6.34	6.32	6.34	6.32
	Magnesite	2.18	1.92	2.20	1.94	2.19	1.94
	Iron containing	2.11	1.41	1.46	0.74	1.42	0.73
4N2 Ca-rich	Calcite	61.5	60.1	61.8	60.3	61.8	60.3
	Magnesite	17.9	15.8	18.0	15.8	18.0	15.8
	Quartz/feldspar	11.5	11.4	11.5	11.5	11.5	11.5
	Ammonium sulfate	8.05	12.0	8.08	12.1	8.07	12.1
	Iron containing	1.07	0.71	0.74	0.37	0.71	0.36

with Asian dust, little is known of the presence of magnetite in Asian dust (X. L. Zhang et al., 2015). Magnetite is a common iron oxide in igneous and metamorphic rocks. It is associated with metamorphic dolomite rock (Anthony et al., 2016) and carbonate sedimentary deposits as a skarn, that is, the intrusion of magnetite-containing magma in sedimentary rock (Deer et al., 2013). The mass percent of iron oxide among the Asian dust particles in this study was 0.6% to 8.1% (average of 2.01% for hematite and 2.0% for magnetite), which spans the reported free iron oxide concentration in Asian dust (3.7%; Lafon et al., 2004) as mentioned earlier.

3.3.1. Ca-Mg Particles

Table 3 shows the percent composition of the mineral phases in the Ca-Mg particles with the iron phase as ankerite, hematite, or magnetite in the first four particles (1D, 2N, 3N, and 4N1). The percent mass of individual oxides is shown in Table S2 in the supporting information. Ankerite occupied 1.4% to 3.8% of the particle volume while magnetite and hematite occupied smaller volumes, 0.3% to 0.8%. For particle 4N2 which contained soot, K mapped with Fe and Si. The particle's K_2O/FeO ratio was 0.19 suggesting the presence of a Fe- and K-rich mica such as annite ($K_2O/FeO = 0.22$; Anthony et al., 2016). Biotites such as annite may form from the metamorphism of dolomitic deposits containing silicon (Deer et al., 2013).

Among the five particles, dolomite occupied the largest volume at 37% to 80%. In the first four particles, the number of Mg atoms exceeded Ca (Figures 5a–5e). Excess Mg was determined as magnesite ($MgCO_3$) with 4.9% to 21% of the volume. Magnesite commonly associates with dolomite in metamorphic rock (Anthony et al., 2016). Dolomite is sometimes described as alternating layers of calcite and magnesite (Deer et al., 2013).

For particles 1D–3N, element maps for Si and Al showed these elements coinciding, suggesting an aluminosilicate phase. Among all five particles, the Al_2O_3/SiO_2 ratio was 0.26 to 0.43. In three of the five particles, Na and K mapped to some extent with Al and Si; however, the Na_2O/SiO_2 ratio was typically higher than the K_2O/SiO_2 ratio. Oxide ratios suggest either a feldspar such as orthoclase or albite ($Al_2O_3/SiO_2 = 0.30$ to

Table 5
Mass and Volume Percent of Mineral Phases in Ca-S Marine Background Air Particles

Particle	Mineral phase	Mass percent	Volume percent
1D Ca-S	Gypsum	89.9	91.5
	Calcite	4.75	4.13
	Quartz	1.85	1.65
	Albite	0.98	0.89
	Magnesite	1.90	1.49
	Hematite	0.66	0.30
2N Ca-S	Gypsum	89.1	90.8
	Calcite	5.23	4.56
	Albite	3.80	3.45
	Magnesite	0.99	0.78
	Hematite	0.93	0.42
	3D Ca-S	Gypsum	83.9
Calcite	1.52	1.32	
Albite (K-feldspar)	12.0	11.0	
Magnesite	2.49	1.96	
Hematite	0	0	
4N Ca-S	Gypsum	89.0	90.5
	Calcite	3.83	3.33
	Quartz	4.93	4.39
	Anorthite	0.57	0.49
	Magnesite	1.65	1.30
	Hematite	0	0

0.31) or a clay such as montmorillonite ($Al_2O_3/SiO_2 = 0.35$; Deer et al., 2013). Clay grains can be nanoparticulate in size (Deer et al., 2013) are often associated with carbonate sedimentary minerals (Anthony et al., 2016) and therefore can be sequestered in a larger dolomite dust particle. Smectite minerals such as montmorillonite were found most abundant in dust during severe storms in Beijing during 2000 and 2002 (Shi et al., 2005). Since Na was more abundant than K in particles 1D, 2N, and 3D, we assign montmorillonite as the aluminosilicate in the Ca-Mg particles, accounting for 6.5% to 20% of the volume.

Sulfur was relatively low and/or not associated with a distinctive spatial feature in Ca-Mg particles 1D, 2N, 3D, and 4N2. For these particles, sulfur was assumed to be a secondary ammonium sulfate phase on the particle's surface from SO_2 oxidation, occupying 1.4% to 5.8% of the total volume. Ammonium sulfate has been shown to be internally mixed with Asian dust (Sullivan et al., 2007). The distinctive sulfur phase in particle 4N1 was assigned as gypsum, occupying 18% of the particle volume.

3.3.2. Ca-Rich Particles

The composition of the mineral phases in the Ca-rich particles with the iron phase as siderite, hematite, or magnetite is shown in Table 4. The percent mass for individual oxides is shown in Table S3 in the supporting information. Siderite occupied 0.7% to 7.8% of the particle volume. As with the Ca-Mg particles, magnetite and hematite occupied smaller volumes, 0.4% to 4.2%. Calcite occupied the largest volume (>60%) in four of the five particles. For particle 2N, gypsum was determined as the larger phase with 57% of the volume followed by calcite at 32%. Occasional

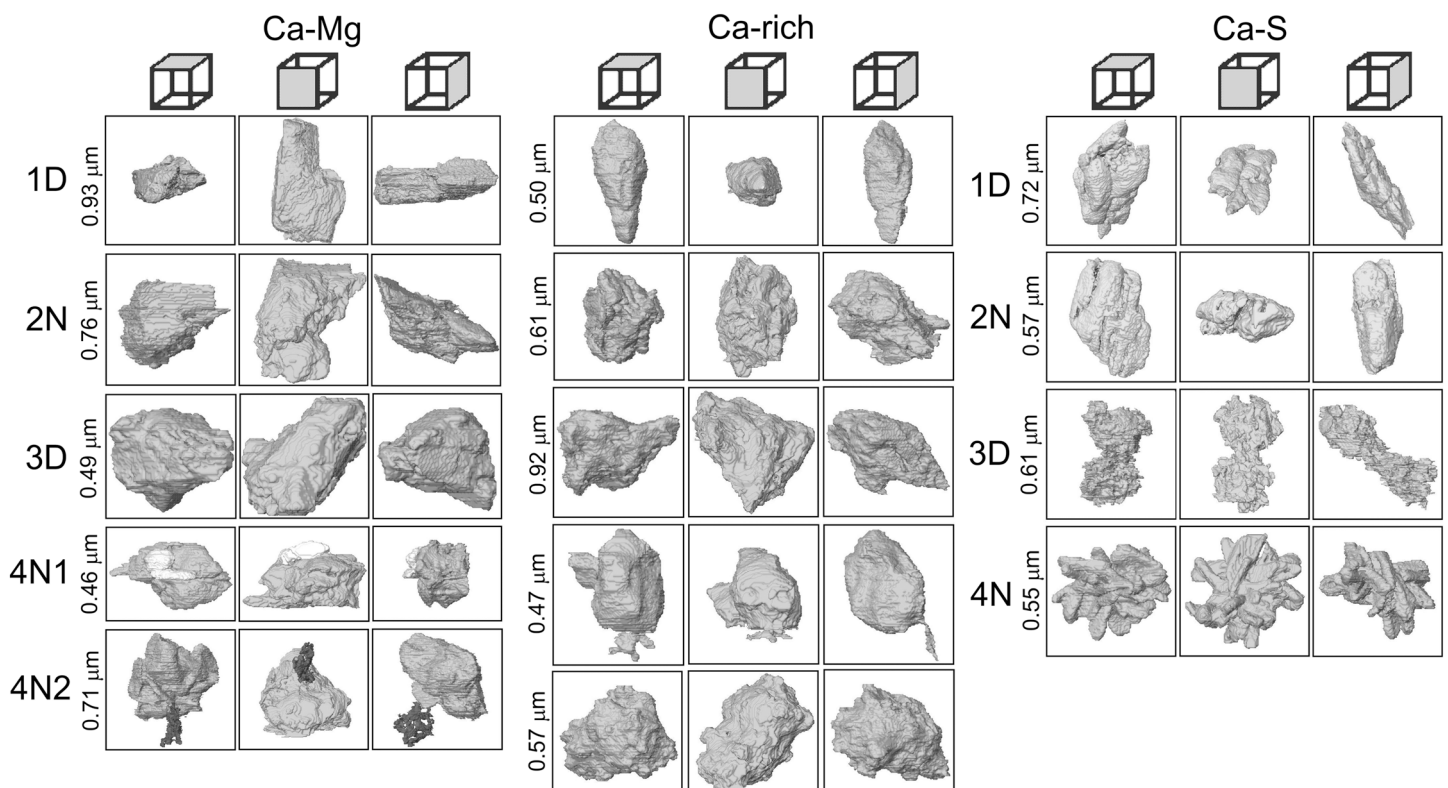


Figure 6. Spatial models from focused ion-beam tomography of Ca-Mg and Ca-rich Asian dust particles 1D to 4N2 and Ca-S background marine air particles 1D to 4N. Dimensions in micrometers are the radii for particles as size-equivalent spheres.

Table 6
Minimum and Maximum Values for Complex Refractive Indices

Particle Class	Particle	Absorbing or nonabsorbing phase	Minimum refractive index		Maximum refractive index			
			Real	Imaginary	Real	Imaginary		
Ca-Mg	1D	Magnetite	1.504	1.53E−03	1.671	1.73E−03		
		Hematite	1.505	1.69E−04	1.673	1.73E−04		
		Ankerite	1.502	4.68E−06	1.670	4.73E−06		
	2 N	Magnetite	1.507	3.20E−03	1.652	3.57E−03		
		Hematite	1.509	3.51E−04	1.656	3.52E−04		
		Ankerite	1.503	8.33E−06	1.650	8.41E−06		
	3D	Magnetite	1.505	2.37E−03	1.662	2.67E−03		
		Hematite	1.507	2.60E−04	1.665	2.63E−04		
		Ankerite	1.502	6.01E−06	1.660	6.07E−06		
	4N1	Magnetite	1.510	5.08E−03	1.653	5.67E−03		
		Hematite	1.513	5.47E−04	1.658	5.56E−04		
		Ankerite	1.503	1.18E−05	1.649	1.19E−05		
	4N2	(^a)	1.509	3.13E−05	1.652	3.21E−05		
		Ca-rich	1D	Magnetite	1.504	5.53E−03	1.642	6.15E−03
				Hematite	1.507	5.94E−04	1.647	6.02E−04
Siderite	1.498			1.16E−05	1.640	1.16E−05		
2N	Magnetite		1.520	4.03E−03	1.569	4.20E−03		
	Hematite		1.522	4.42E−04	1.573	4.01E−04		
	Siderite		1.515	6.80E−06	1.567	6.76E−06		
3D	Magnetite		1.532	2.14E−02	1.660	2.36E−02		
	Hematite		1.544	2.32E−03	1.681	2.28E−03		
	Siderite		1.508	1.34E−05	1.648	1.34E−05		
4N1	Magnetite		1.503	3.57E−03	1.632	3.94E−03		
	Hematite		1.505	3.96E−04	1.636	3.91E−04		
	Siderite		1.499	6.89E−06	1.630	6.85E−06		
4N2	Magnetite		1.503	1.83E−03	1.640	2.03E−03		
	Hematite		1.505	2.01E−04	1.642	2.00E−04		
	Siderite		1.501	5.63E−06	1.640	5.59E−06		
Ca-S	1D	Hematite	1.523	1.62E−04	1.542	1.43E−04		
		Hematite	1.524	2.27E−04	1.542	2.00E−04		
	3D	(^b)	1.521	5.71E−06	1.536	5.72E−06		
	4N	(^b)	1.521	2.33E−06	1.538	2.32E−06		

Note. Determined from Maxwell-Garnett dielectric function, equation (1).

^aSoot phase is not included in Maxwell-Garnett dielectric function. ^bNo iron-containing phase was detected.

substitution of Mg atoms for Ca atoms in calcite is common (hence, as MgCO₃; Deer et al., 2013). Therefore, magnesium in each particle was assigned as magnesite.

Among particles 1D, 2N, and 3D, the Al₂O₃/SiO₂ ratio was 0.35 to 0.52 resembling a smectite or the feldspar albite, perhaps in solution with anorthite. However, Na₂O/SiO₂ ratios were relatively high (0.14 to 0.37) and far closer to the ratio for albite (0.16) than, for example, montmorillonite (<0.04; Deer et al., 2013). For 1D, 2N, and 3D, the phase was assigned as albite. For particles 4N1 and 4N2, Al concentrations were low, and Al₂O₃/SiO₂ was 0.14 and 0.4 respectively; Na and K were barely detected, and thus, the silicate phase was likely quartz with perhaps some anorthite. For 4N1 and 4N2, the silicate was assigned quartz.

As with the Ca-Mg particles, the sulfur phase in the Ca-rich particles was assumed to be ammonium sulfate at low S concentrations or when not associated with a structural feature (particles 1D and 4N2). For 3D and 4N1, the phase was assigned gypsum.

3.3.3. Ca-S Particles

The predominant phase in the Ca-S particles, as gypsum, comprised a far larger part of volume in each of the four particles, 86% to 92%, compared to the predominant phase in the Asian dust particles (Table 5). Other minerals in the Ca-S particles were assigned as feldspar albite or anorthite with a volume of 0.5% to 11%, quartz with 1.6% to 4.9%, calcite with 1.3% to 4.6%, and magnesite with 0.8% to 2%. The iron phase

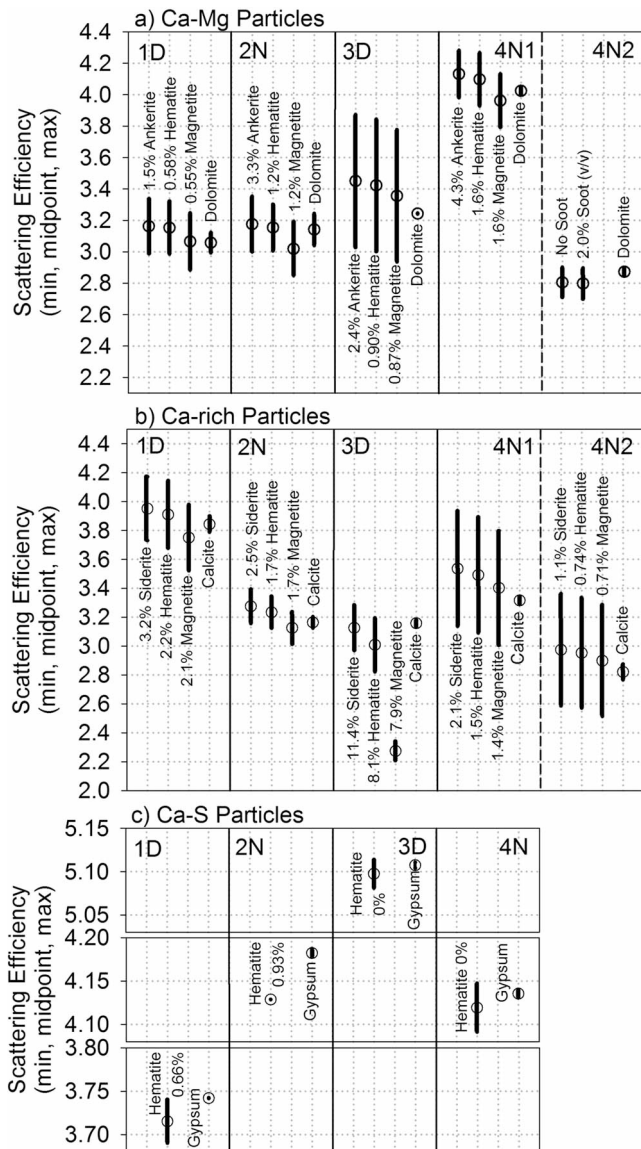


Figure 7. Scattering efficiency for Ca-Mg and Ca-rich Asian dust particles and Ca-S background marine air particles along with size- and shape-equivalent particles of neat dolomite, calcite, and gypsum, respectively. Vertical bars indicate the scattering range. Open circles indicate the range midpoint. Except for Ca-Mg particle 4N2, the iron-containing phase composition is mass percent.

volume was nearly negligible (<0.5%) and was assigned hematite. The percent mass for individual oxides are shown in Table S4 in the supporting information.

3.4. Spatial Models

Three-dimensional reconstructions of the 10 Asian dust particles and 4 marine background air particles from FIB tomography are shown in Figure 6. Compared with the secondary electron images in Figure 5, it is apparent that the 3-D reconstructions accurately represent particle shape and surface features. Particle volume was determined from the 3-D reconstruction of the whole particle rather than as the cumulative volume of the particle's mineral phases. Volumes for the Ca-Mg, Ca-rich, and Ca-S particles, averaged 1.50 ± 1.19 ($\bar{x} \pm s$), 1.19 ± 1.18 , and $0.99 \pm 0.39 \mu\text{m}^3$, respectively. The spatial models are not shown to scale in Figure 6; however, the figure shows the effective radius (i.e., as a volume-equivalent sphere) of each particle. Average diameters for the Ca-Mg, Ca-rich, and Ca-S particles were similar: 1.33 ± 0.39 ($\bar{x} \pm s$), 1.23 ± 0.36 , and $1.22 \pm 0.15 \mu\text{m}$, respectively.

3.5. Optical Models

Complex refractive indices from the Maxwell-Garnett dielectric function (equation (1)) for the Asian dust and Ca-S marine background air particles are shown in Table 6. Refractive indices for the individual mineral phases as input to equation (1) (transformed as dielectric constants) for each particle are shown in Tables S5 to S7 in the supporting information. Figure 7 shows scattering behavior for the particles. For the Asian dust, we compare the heterogeneous particles containing the nonabsorbing phase (e.g., iron carbonate) and the absorbing phase (e.g., hematite or magnetite) with size- and shape-equivalent neat dolomite or calcite. Since the Ca-Mg 4N2 particle contained soot, Figure 7 shows the particle with or without soot compared with an equivalent dolomite particle. Shown also in Figure 7 are the mass concentrations of the iron-containing phases (or volume concentration for the soot in Ca-Mg 4N2).

The main observation from Figure 7 is that individual Asian dust particles generally exhibit a much wider scattering range than equivalent dolomite and calcite particles. This is the result of a variety of possible spatial orientations for the anisotropic phases in a heterogeneous particle (see Figure 1), and thus a wider range of refractive indices, than for neat particles with a single anisotropic phase. We refer to this disparity in the extent of scattering between Asian dust and neat-phase particles as the heterogeneity factor.

Figure 8 shows heterogeneity factors for extinction, scattering, and the backscatter fraction in this study. The factor is calculated as the range of an optical property for an Asian dust particle divided by the range for an equivalent neat-phase particle. Excluding the soot-containing Ca-Mg particle 4N2, heterogeneity factors in Figure 8 are an average that includes particles with absorbing hematite, magnetite, and the nonabsorbing iron carbonate (ankerite or siderite). As Figure 8 shows, the extent that extinction, scattering, and backscattering vary due to the possible orientations of the anisotropic phases in a heterogeneous particle may be many times greater than the extent these properties vary for an equivalent homogeneous particle. Nevertheless, at the concentrations of iron found in these particles, whether a heterogeneous particle contains an absorbing iron oxide or nonabsorbing iron carbonate, appears to make little difference. Rather, the extent that extinction, scattering, and backscattering vary in a heterogeneous particle likely depends on the more abundant nonabsorbing phases in the particles such as a clay or feldspar mineral.

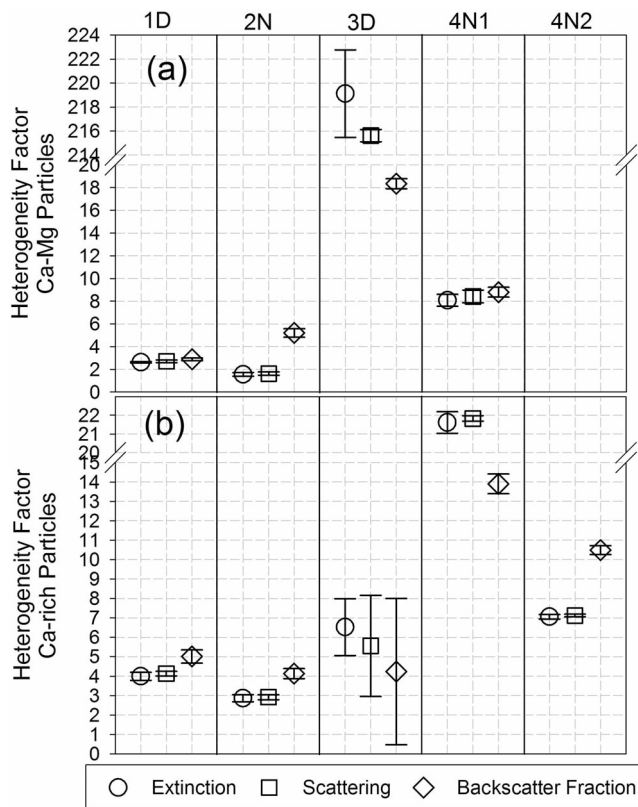


Figure 8. (a, b) The heterogeneity factor is the extent that extinction, scattering, or backscatter fraction varies for a heterogeneous particle due to the spatial arrangement of phases relative to that for a neat-phase dolomite or calcite particle. It is the range of an optical property for a heterogeneous particle divided by the range for the corresponding neat particle. Circles, squares, and diamonds indicate the average for particles containing the different iron-containing phases; error bars indicate standard deviation. The soot-containing Ca-Mg 4N2 particle is not shown.

Along with the extent of variation in scattering efficiencies, Figure 7 shows the range midpoints (open circles). We use the midpoint as surrogate for the average optical behavior of a population of particles with the same composition. Based on midpoints as further discussed below (and shown in Figure 9), scattering and extinction tend to be higher for the heterogeneous particles than the respective neat dolomite or calcite particles. This is most evident for particles with nonabsorbing iron carbonate (ankerite or siderite) than with iron oxide.

Interestingly, scattering as well as extinction (not shown in Figure 7) tend to be lower for the heterogeneous Ca-S marine background air particles than the equivalent neat gypsum particles, hence, opposite from the Asian dust particles. Since iron was negligible or nonexistent in the Ca-S particles, the difference here between the heterogeneous Ca-S particles and equivalent neat gypsum particles is due to the radiative interactions involving the noniron phases (e.g., calcite, feldspar, or quartz) and the larger gypsum matrix.

Figure 9 shows the midpoints of the ranges for extinction, scattering, and the backscatter fraction for the Asian dust particles versus their effective radii, which range from 0.46 to 0.93 μm . The Ca-Mg particles (excluding soot-containing 4N2) are shown in panels (a), (c), and (e); Ca-rich particles are shown in panels (b), (d), and (f). Regardless of composition, extinction and scattering appear to decrease with particle size in general, which would be expected for spherical Mie-sized particles with the same composition and mass concentration. However, we cannot determine that particle size is a controlling factor affecting extinction and scattering given the limited number of particles studied. Nevertheless, there is generally more variation between particles than between the iron phase treatments for each particle and the neat particle (dolomite or calcite) in each case. This indicates that variation in extinction, scattering, and the backscatter fraction among the Asian dust particles in this study is due to morphology or size rather than composition.

3.5.1. Extinction Efficiencies

Among the Ca-Mg particles, the extinction efficiencies with ankerite, hematite, and magnetite phases shown in Figure 9 are similar, ranging from 3.16 to 4.13, 3.16 to 4.11, and 3.16 to 4.09, respectively. The average among the three iron phase treatments is 3.47 ± 0.40 ($\bar{x} \pm s$, $n = 12$). Not shown in Figure 9 is the extinction efficiency for the Ca-Mg particle with soot (4N2), which was lower at 2.97. For the Ca-rich particles, extinction efficiencies with siderite, hematite, and magnetite phases in Figure 9 are also similar, ranging from 2.97 to 3.95, 2.96 to 3.93, and 2.97 to 3.91, respectively. The extinction average among the three treatments for the Ca-rich particles is 3.36 ± 0.35 ($\bar{x} \pm s$, $n = 15$). Among all Asian dust particles and treatments, extinction averaged 3.39 ± 0.37 ($\bar{x} \pm s$, $n = 28$).

Among the Ca-S marine background air particles, extinction was higher, ranging from 3.72 to 5.10 and averaging 4.27 ± 0.58 ($\bar{x} \pm s$, $n = 4$). Two-tailed t tests indicate that the Ca-Mg and Ca-rich particles are not statistically different with respect to extinction ($H_1 : \bar{x}_1 \neq \bar{x}_2$, $Pr \geq 0.45$). There is, however, a high probability that extinction for the marine background air particles is different from both the Ca-Mg particles ($H_1 : \bar{x}_1 \neq \bar{x}_2$, $Pr \geq 0.94$) and the Ca-rich particles ($H_1 : \bar{x}_1 \neq \bar{x}_2$, $Pr \geq 0.95$). In summary, extinction with the Asian dust particles was 19% to 21% lower than extinction with the marine background air particles.

Figure 9 also shows that extinction efficiencies are generally higher for the heterogeneous particles than the neat-phase particles for both the Ca-Mg and Ca-rich particles. For the Ca-Mg particles, extinction increases by 3.4%, 3.1%, and 3.0% on average with ankerite, hematite, and magnetite, respectively, relative to the equivalent dolomite particles. For the Ca-rich particles, extinction increases by 3.0%, 2.5%, and 2.4% on average with siderite, hematite, and magnetite relative to equivalent calcite particles.

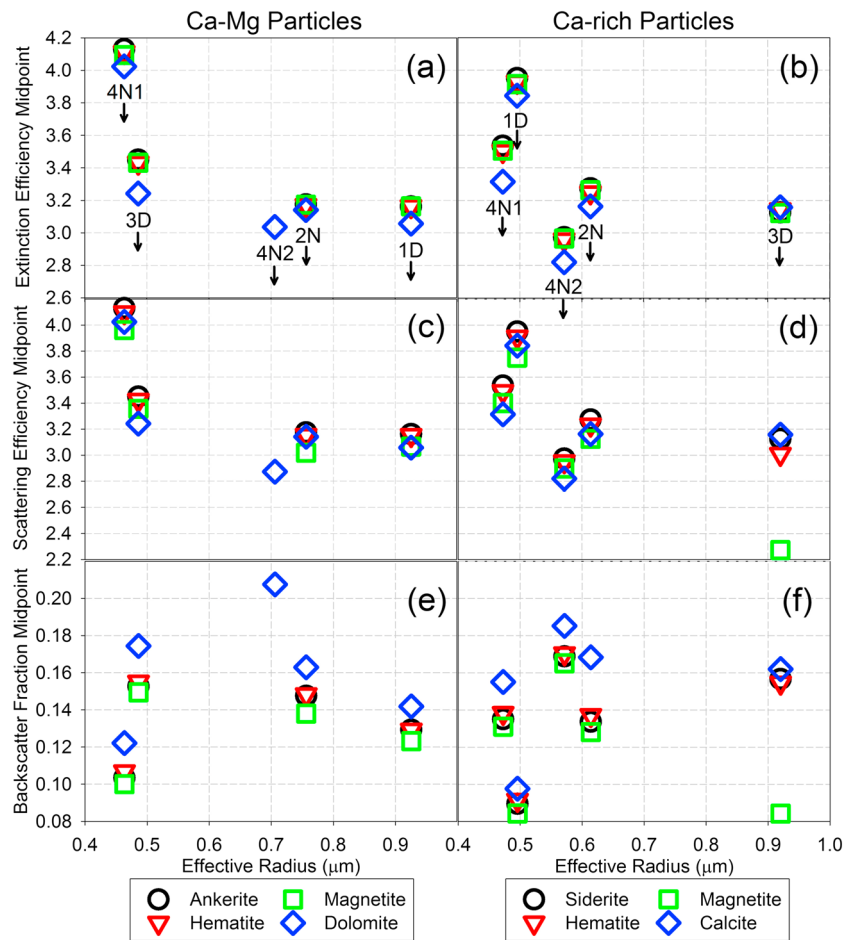


Figure 9. Range midpoints for extinction and scattering efficiencies and the backscatter fraction for Asian dust particles with hematite, magnetite, or a nonabsorbing iron carbonate (ankerite or siderite) and for size- and shape-equivalent neat particles. Panels (a), (c), and (e) are Ca-Mg particles. Panels (b), (d), and (f) are Ca-rich particles.

3.5.2. Scattering Efficiencies

Among the Ca-Mg particles in Figure 9, scattering efficiencies with ankerite, hematite, and magnetite phases range from 3.16 to 4.13, 3.15 to 4.10, and 3.02 to 3.96, respectively. The scattering average among the three iron phase treatments is 3.43 ± 0.41 ($\bar{x} \pm s$, $n = 12$). For the Ca-rich particles, scattering efficiencies with siderite, hematite, and magnetite range from 2.97 to 3.95, 2.95 to 3.91, and 2.27 to 3.75, respectively, and average 3.26 ± 0.44 ($\bar{x} \pm s$, $n = 15$) among the three treatments.

With hematite or magnetite mass concentrations in the Ca-Mg particles as low as 0.6%, the effect on scattering by higher absorbing magnetite versus the nonabsorbing iron carbonate or even versus less absorbing hematite is evident. For example, a two-tailed t test indicates that the average difference in scattering efficiencies between Ca-Mg particles with magnetite and ankerite ($\bar{x}_1 = 0.13$) is statistically significant from the average difference in scattering between particles with hematite and ankerite ($\bar{x}_2 = 0.02$) ($H_1 : \bar{x}_1 \neq \bar{x}_2$, $\text{Pr} \geq 0.99$). The effect is similarly observed for the Ca-rich particles. Excluding particle 3D with its relatively high iron content, the average difference in scattering efficiencies between Ca-rich particles with magnetite and siderite ($\bar{x}_1 = 0.14$) is statistically significant from the average difference in scattering between particles with hematite and siderite ($\bar{x}_2 = 0.04$) ($H_1 : \bar{x}_1 \neq \bar{x}_2$, $\text{Pr} \geq 0.97$).

We also observe differences in scattering efficiencies between the Asian dust particles and the equivalent neat-phase particles at the low iron phase concentrations in this study. Scattering by the Ca-Mg particles with ankerite and hematite was higher by 3.4% and 2.7%, respectively, than the equivalent dolomite particles. However, scattering with magnetite was slightly lower (by 0.4%) than the equivalent dolomite

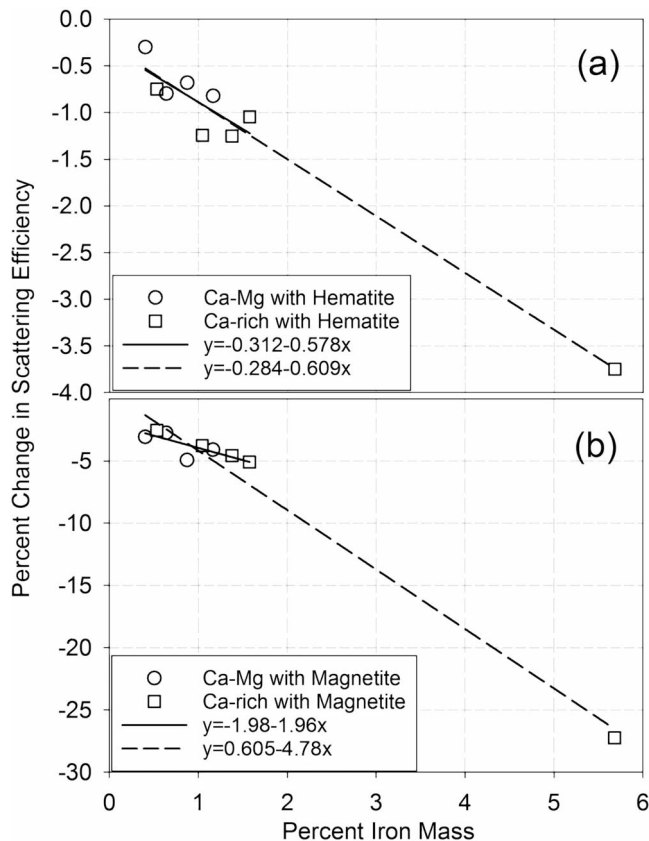


Figure 10. Percent change in the scattering efficiency versus iron mass and first-order regression models. (a) Asian dust with hematite; b Asian dust with magnetite. Solid-line regression excludes the outlier Ca-rich particle (3D) with high iron mass. Dashed-line regression includes the outlier.

particles. For the Ca-rich particles containing magnetite, scattering was substantially lower on average than the equivalent calcite particles, by 7.2%. However, this was driven largely by the relatively high iron content of particle 3D. Excluding particle 3D, scattering was only slightly lower (by 0.3%) than the equivalent calcite particles. Scattering with siderite and hematite in the Ca-rich particles was higher by, 3.0% and 1.1%, similar to the Ca-Mg particles.

The effect on the scattering efficiency due to absorbing iron versus non-absorbing iron can be further quantified if we consider that the effect of iron oxide on the Ca-Mg and Ca-rich particles is similar. Figure 10 shows the percent change in scattering versus iron mass for the Asia dust particles with iron oxide relative to particles with iron carbonate. The decrease in scattering with iron mass is comparable between the Ca-Mg (open circles) and Ca-rich (open squares) particles and can be approximated with a first-order function. The solid-line regression line includes all Asian dust particles except for the outlier with 5.8% Fe mass (particle 3D), while the dashed-line regression includes the outlier. For the Asian dust with hematite (Figure 10a), scattering efficiency decreased at 0.58% to 0.61% with a 1% increase in iron mass. For Asian dust with magnetite (Figure 10b), scattering efficiency decreased as expected at a much greater rate, 2.0% to 4.8% with a 1% increase in iron mass.

3.5.3. Backscatter Fraction

All Asian dust particles in this study strongly scattered light forward. The backscatter intensity fraction shown in Figure 9 for the Asian dust overall ranges from 0.084 to 0.17. The backscatter fraction for the Ca-Mg 4N2 particle with soot (not shown in Figure 9) was larger at 0.19. Among the Ca-Mg particles, the backscatter fraction with ankerite, hematite, and magnetite phases ranged from 0.10 to 0.16 and averaged 0.13 ± 0.02 ($\bar{x} \pm s$, $n = 12$). The backscatter fraction for the Ca-rich particles with siderite, hematite, and magnetite had a slightly wider range, 0.084 to 0.17, but averaged the same as the Ca-Mg particles: 0.13 ± 0.03 ($\bar{x} \pm s$, $n = 15$). For the Ca-S marine background air particles, the backscatter fraction averaged 0.085 ± 0.01 ($\bar{x} \pm s$, $n = 4$). Two-tailed t tests indicated a high probability that the marine background air particles are statistically different from both the Ca-Mg and Ca-rich particles ($H_1: \bar{x}_1 \neq \bar{x}_2$, $Pr \geq 0.99$). Thus, the backscattering among all Asian dust particles in this study was 56% higher than for the marine background air particles.

An interesting observation from Figure 9 is that the backscatter fraction of the Asian dust particles is invariably lower than that of the equivalent neat phase dolomite and calcite particles. The effect is tied to the type of iron-containing phase. For the Ca-Mg particles, the backscatter fraction on average is 15% lower with magnetite, 10% lower with hematite, and 11% lower with ankerite than the equivalent dolomite particles. Similarly, the backscatter fraction for the Ca-rich particles is on average 25% lower with magnetite, 10% lower with hematite, and 11% lower with siderite than the equivalent calcite particles. These results suggest that the backscatter fraction is inversely related to the magnitude of the imaginary part of the complex refractive index, that is, the type of iron oxide phase, as reported by others (Flores et al., 1998).

3.5.4. SSA

SSA for the Asian dust particles with the absorbing phases is shown in Figure 11. (SSA for Asian dust with nonabsorbing ankerite or siderite is >0.99 and is not shown in Figure 11.) For the Ca-Mg particles with hematite, SSA was >0.99 , similar to that for particles with ankerite. Thus, hematite with mass concentrations $\leq 1.6\%$ had little effect on SSA. For particles with magnetite, also at mass concentrations $\leq 1.6\%$, SSA averaged 0.96 ± 0.01 ($\bar{x} \pm s$, $n = 4$). For the 4N2 particle with soot (2% by volume), SSA was slightly lower at 0.94.

With one exception (particle 3D), SSA for the Ca-rich particles with hematite and magnetite resembled those for the Ca-Mg particles. As noted above, the iron concentration of particle 3D far exceeded that of the other

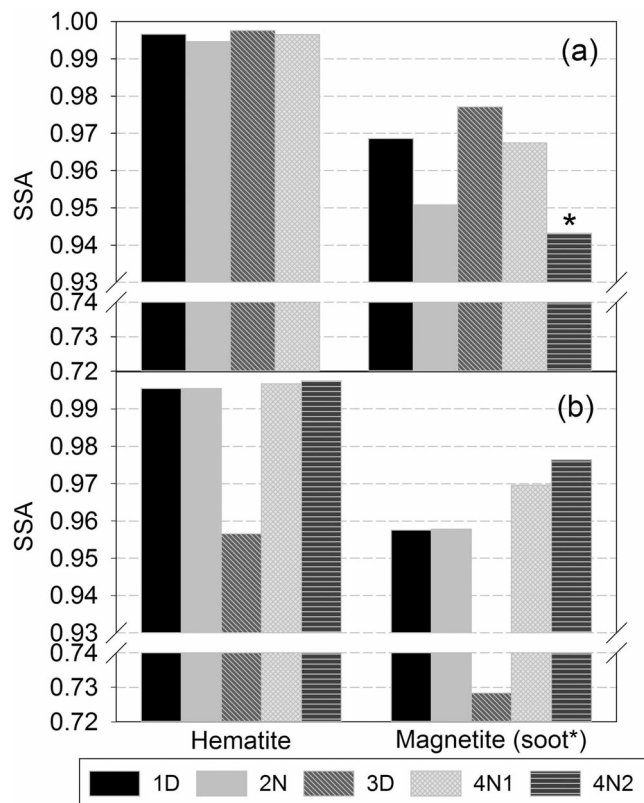


Figure 11. Single scattering albedo for Ca-Mg (a) and Ca-rich (b) particles. SSA = single scattering albedo.

particles. Nevertheless, the effect was far greater with magnetite than hematite. SSA for particle 3D with hematite was 0.96, but the SSA average for Ca-rich particles with hematite, including particle 3D, was 0.99, similar to that for particles with siderite. In contrast, SSA for particle 3D with magnetite was 0.72, bringing the SSA average for all Ca-rich particles with magnetite to 0.92 ± 0.11 ($\bar{x} \pm s$, $n = 5$). Among all Asian dust particles with iron oxide or soot, SSA averaged 0.96 ± 0.06 ($\bar{x} \pm s$, $n = 19$). Based on the regressions shown in Figure 10, we would expect SSA of heterogeneous Asian dust with hematite to decrease by 0.6% and magnetite by 2% to 4.8% with a 1% increase in iron mass.

The average SSA reported here (0.96 ± 0.06) for heterogeneous dust with iron oxide or soot is comparable to median values of 0.943 and 0.969 measured by aethalometers at MLO during March and April 1992 (Bodhaine, 1995). An SSA of approximately 0.96 was also determined for April 2006 from AEROSOL ROBOTICS NETWORK retrievals at Dalanzadgad, Mongolia (43.3° N, 104.3° E), a site in the Gobi desert (Su & Toon, 2011).

Nevertheless, some studies have determined a lower SSA for Asian dust. For example, Lee et al. (2007) determined an average SSA across China in 2005 of 0.89 ± 0.04 for $0.55 \mu\text{m}$ light from ground-based transmittance measurements and reflected spectral radiances from the Moderate Resolution Imaging Spectroradiometer onboard National Aeronautics and Space Administration's Terra satellite. However, ground-based SSA determinations from the Lee et al. study taken from March to May were much higher (0.94 and 0.96) at desert sites in northern China (Eerduosi and Shapotou). Another study showed lower SSA values of 0.918 and 0.913 with $0.5\text{-}\mu\text{m}$ light during March through May at Dunhuang, a site east of the Taklimakan desert and at

Mandalgovi, an arid site north of the Gobi desert, respectively (Kim et al., 2004). In contrast, Ge et al. (2010) reported average SSAs of 0.75 for $0.500\text{-}\mu\text{m}$ light and 0.80 for $0.615\text{-}\mu\text{m}$ light from ground-based measurements taken during April to June 2008 at Zhangye, a semidesert site south of the Gobi desert. It has been suggested that the lower SSA values at Zhangye may be due to local pollution (Su & Toon, 2011).

4. Conclusions

In this study, we have used microanalytical and 3-D modeling techniques to show how extinction, scattering, SSA, and the backscatter fraction for individual heterogeneous Asian dust particles sampled at MLO vary with composition. Two types of Asian dust particles were identified: Ca-Mg particles, which largely contained dolomite, and Ca-rich particles, which largely contained calcite. We focused for the most part on the effect a minor iron-containing phase has on particle optical behavior, either an absorbing iron oxide (hematite or magnetite) or a nonabsorbing iron carbonate (ankerite or siderite). Optical properties of the heterogeneous particles were compared with particles of identical size and shape but consisting of a neat mineral phase (dolomite or calcite). We also compared the Asian dust optical properties with those of marine background air at MLO.

In general, variation in extinction, scattering, and the backscatter fraction among the Asian dust particles was likely due more to morphology or size than composition. For the mass concentrations of iron (0.4% to 5.8%) in the two types of Asian dust particles studied here, the type of iron-containing phase had little effect on extinction. However, average extinction efficiencies for the Ca-Mg and Ca-rich particles, 3.47 and 3.36, respectively, were 19% to 21% lower than that of the marine background air particles (3.72). By contrast, the extinction efficiencies for the Asian dust were consistently higher, albeit by a modest 2.4% to 3.4%, than extinction for the size- and shape-equivalent neat dolomite and calcite particles.

The presence of an iron oxide had a noticeable effect on scattering in the Asian dust particles compared to the nonabsorbing iron carbonate even at the low iron oxide mass concentrations studied here (0.6% to 8.1%). For example, the average scattering efficiency for Ca-rich particles with magnetite (3.09) was sharply lower than with siderite and hematite (3.37 and 3.32). Scattering efficiency decreased by <1% with a 1% increase in hematite mass but decreased by 2% to 5% with an increase in magnetite mass.

As expected, the Asian dust particles strongly scattered light forward, with the backscatter fraction averaging 0.12 to 0.13. However, forward scattering by the marine background air particles was even stronger. Backscattering by Asian dust particles was 56% higher than backscattering by the marine background particles.

Backscattering was invariably lower in the Asian dust particles than the equivalent neat-phase particles. However, the extent of backscattering also depended on type of iron-containing phase. The backscatter fraction averaged 15% to 25% lower with magnetite but only 10% to 11% lower with hematite or iron carbonate. The result corroborates reports that an absorptive iron oxide, that is, with a large imaginary complex refractive index, decreases backscattering or, conversely, increases forward scattering.

At the concentrations of iron studied here, the presence of hematite in the Asian dust had a negligible effect on SSA, for the most part, compared to the particles with iron carbonate. However, this was not the case with magnetite. At the highest iron concentration, 5.8%, SSA with hematite was 0.92, but 0.72 with magnetite. By comparison, the Ca-Mg particle with 2% soot by volume had an SSA of 0.94. The average SSA for all particles with either hematite, magnetite, or soot was 0.96 ± 0.06 , comparable to or within range of SSA reported by others for Asian dust.

Acknowledgments

We thank Aidan Colton of the National Oceanic and Atmospheric Administration, Hilo, Hawaii for assistance in aerosol sampling at MLO. Supporting data are contained in three figures and seven tables in the supporting information. Additional data are available at the website (<https://doi.org/10.18434/T4/1503344>).

References

- Anthony, J. W., Bideaux, R. A., Bladh, K. W., & Nichols, M. C. (Eds.) (2016). *Handbook of mineralogy*. Chantilly, VA: Mineralogical Society of America. Retrieved from <http://www.handbookofmineralogy.org/>
- Bloss, F. D. (1961). *An introduction to the methods of optical crystallography* (pp. 65–91). New York: Holt, Rinehart and Winston.
- Bodhaine, B. A. (1995). Aerosol absorption-measurements at Barrow, Mauna-Loa and the south-pole. *Journal of Geophysical Research*, *100*(D5), 8967–8975. <https://doi.org/10.1029/95JD00513>
- Bodhaine, B. A., Mendonca, B. G., Harris, J. M., & Miller, J. M. (1981). Seasonal-variations in aerosols and atmospheric transmission at Mauna Loa Observatory. *Journal of Geophysical Research*, *86*(NC8), 7395–7398. <https://doi.org/10.1029/JC086iC08p07395>
- Bohren, C. F., & Huffman, D. R. (1983). *Absorption and scattering of light by small particles*. Weinheim: Wiley-VCH Verlag GmbH & Co. KGaA.
- Bohren, C. F., & Wickramasinghe, N. C. (1977). On the computation of optical properties of heterogeneous grains. *Astrophysics and Space Science*, *50*(2), 461–472. <https://doi.org/10.1007/bf00641750>
- Boucher, O., Randall, D., Artaxo, P., Bretherton, C., Feingold, G., Forster, P., et al. (2013). Clouds and Aerosols. In T. F. Stocker, D. Qin, G.-K. Plattner, M. Tignor, S. K. Allen, J. Boschung, et al. (Eds.), *Climate Change 2013: The Physical Science Basis. Contribution of Working Group I to the Fifth Assessment Report of the Intergovernmental Panel on Climate Change* (pp. 571–658). Cambridge, UK and New York: Cambridge University Press. <https://doi.org/10.1017/CBO9781107415324.016>
- Braaten, D. A., & Cahill, T. A. (1986). Size and composition of Asian dust transported to Hawaii. *Atmospheric Environment*, *20*(6), 1105–1109. [https://doi.org/10.1016/0004-6981\(86\)90142-3](https://doi.org/10.1016/0004-6981(86)90142-3)
- Cao, J. J., Lee, S. C., Zhang, X. Y., Chow, J. C., An, Z. S., Ho, K. F., et al. (2005). Characterization of airborne carbonate over a site near Asian dust source regions during spring 2002 and its climatic and environmental significance. *Journal of Geophysical Research*, *110*, D03203. <https://doi.org/10.1029/2004JD005244>
- Choobari, O. A., Zawar-Reza, P., & Sturman, A. (2014). The global distribution of mineral dust and its impacts on the climate system: A review. *Atmospheric Research*, *138*, 152–165. <https://doi.org/10.1016/j.atmosres.2013.11.007>
- Christensen, J. H. (1997). The Danish Eulerian hemispheric model—A three-dimensional air pollution model used for the Arctic. *Atmospheric Environment*, *31*(24), 4169–4191. [https://doi.org/10.1016/s1352-2310\(97\)00264-1](https://doi.org/10.1016/s1352-2310(97)00264-1)
- Chun, Y. S., Cho, H. K., Chung, H. S., & Lee, M. (2008). Historical records of Asian dust events (hwangsa) in Korea. *Bulletin of the American Meteorological Society*, *89*(6), 823–828. <https://doi.org/10.1175/2008bams2159.1>
- Conny, J. M. (2013). The internal composition of atmospheric dust particles from focused ion-beam scanning electron microscopy. *Environmental Science and Technology*, *47*(15), 8575–8581. <https://doi.org/10.1021/es400727x>
- Conny, J. M., Collins, S. M., & Herzog, A. A. (2014). Qualitative multiplatform microanalysis of individual heterogeneous atmospheric particles from high-volume air samples. *Analytical Chemistry*, *86*(19), 9709–9716. <https://doi.org/10.1021/ac5022612>
- Conny, J. M., & Ortiz-Montalvo, D. L. (2017). Effect of heterogeneity and shape on optical properties of urban dust based on three-dimensional modeling of individual particles. *Journal of Geophysical Research: Atmospheres*, *122*, 9816–9842. <https://doi.org/10.1002/2017jd026488>
- Darzi, M., & Winchester, J. W. (1982). Aerosol characteristics at Mauna-Loa-Observatory, Hawaii, after East Asian dust storm episodes. *Journal of Geophysical Research*, *87*(NC2), 1251–1258. <https://doi.org/10.1029/JC087iC02p01251>
- Deer, W. A., Howie, R. A., & Zussman, J. (2013). *An introduction to rock-forming minerals*. London: The Mineralogical Society.
- Draine, B. T., & Flatau, P. J. (1994). Discrete-dipole approximation for scattering calculations. *Journal of the Optical Society of America*, *11*, 1491–1499.
- Draine, B. T., & Flatau, P. J. (2013). User guide for the discrete dipole approximation code DDSCAT 7.3 (p. 101).
- Draxler, R. R. (1999). HYSPLIT user's guide. In *NOAA Tech. Memo. ERL ARL-230* Silver Spring, MD: NOAA Air Resources Laboratory.

- Engelbrecht, J. P., Moosmuller, H., Pincock, S., Jayanty, R. K. M., Lersch, T., & Casuccio, G. (2016). Technical note: Mineralogical, chemical, morphological, and optical interrelationships of mineral dust re-suspensions. *Atmospheric Chemistry and Physics*, *16*(17), 10,809–10,830. <https://doi.org/10.5194/acp-16-10809-2016>
- Fan, X. B., Okada, K., Niimura, N., Kai, K., Arai, K., Shi, G. Y., et al. (1996). Mineral particles collected in China and Japan during the same Asian dust-storm event. *Atmospheric Environment*, *30*(2), 347–351. [https://doi.org/10.1016/1352-2310\(95\)00271-y](https://doi.org/10.1016/1352-2310(95)00271-y)
- Fitzgerald, E., Ault, A. P., Zauscher, M. D., Mayol-Bracero, O. L., & Prather, K. A. (2015). Comparison of the mixing state of long-range transported Asian and African mineral dust. *Atmospheric Environment*, *115*, 19–25. <https://doi.org/10.1016/j.atmosenv.2015.04.031>
- Flores, O., Claquin, T., & Schulz, M. (1998). *Contribution to the study of atmospheric dust sources: A mineralogical approach* Rep. Hamburg, Germany: University of Hamburg.
- Formenti, P., Schutz, L., Balkanski, Y., Desboeufs, K., Ebert, M., Kandler, K., et al. (2011). Recent progress in understanding physical and chemical properties of African and Asian mineral dust. *Atmospheric Chemistry and Physics*, *11*(16), 8231–8256. <https://doi.org/10.5194/acp-11-8231-2011>
- Ge, J. M., Su, J., Ackerman, T. P., Fu, Q., Huang, J. P., & Shi, J. S. (2010). Dust aerosol optical properties retrieval and radiative forcing over northwestern China during the 2008 China-US joint field experiment. *Journal of Geophysical Research*, *115*, D09202. <https://doi.org/10.1029/2009JD013263>
- Giles, D. M., Holben, B., Slutsker, I., Welton, E. J., Chin, M., Schmaltz, J., et al. (2006). *A new web-based tool for aerosol data analysis: The AERONET data synergy tool*. Greenbelt, MD: NASA Goddard Space Flight Center.
- Greenland, D. J., Oades, J. M., & Sherwin, T. W. (1968). Electron-microscope observations of iron oxides in some red soils. *Journal of Soil Science*, *19*(1), 123–126. <https://doi.org/10.1111/j.1365-2389.1968.tb01526.x>
- Hansen, J., Sato, M., & Ruedy, R. (1997). Radiative forcing and climate response. *Journal of Geophysical Research*, *102*(D6), 6831–6864. <https://doi.org/10.1029/96JD03436>
- Haywood, J., & Boucher, O. (2000). Estimates of the direct and indirect radiative forcing due to tropospheric aerosols: A review. *Reviews of Geophysics*, *38*(4), 513–543. <https://doi.org/10.1029/1999RG000078>
- Haywood, J., Francis, P., Osborne, S., Glew, M., Loeb, N., Highwood, E., et al. (2003). Radiative properties and direct radiative effect of Saharan dust measured by the C-130 aircraft during SHADE: 1. Solar spectrum. *Journal of Geophysical Research*, *108*(D18), 8577. <https://doi.org/10.1029/2002JD002687>
- Hogan, T. F., & Brody, L. R. (1993). Sensitivity studies of the navy global forecast model parameterizations and evaluation of improvements to NOGAPS. *Monthly Weather Review*, *121*(8), 2373–2395. [https://doi.org/10.1175/1520-0493\(1993\)121<2373:ssotng>2.0.co;2](https://doi.org/10.1175/1520-0493(1993)121<2373:ssotng>2.0.co;2)
- Hogan, T. F., & Rosmond, T. E. (1991). The description of the navy operational global atmospheric prediction systems spectral forecast model. *Monthly Weather Review*, *119*(8), 1786–1815. [https://doi.org/10.1175/1520-0493\(1991\)119<1786:tdotno>2.0.co;2](https://doi.org/10.1175/1520-0493(1991)119<1786:tdotno>2.0.co;2)
- Holmes, J., & Zoller, W. (1996). The elemental signature of transported Asian dust at Mauna Loa Observatory. *Tellus Series B-Chemical and Physical Meteorology*, *48*(1), 83–92. <https://doi.org/10.1034/j.1600-0889.1996.00008.x>
- Huang, J. P., Wang, T. H., Wang, W. C., Li, Z. Q., & Yan, H. R. (2014). Climate effects of dust aerosols over East Asian arid and semiarid regions. *Journal of Geophysical Research: Atmospheres*, *119*, 11,398–11,416. <https://doi.org/10.1002/2014jd021796>
- Iwasaka, Y. (2003). Importance of dust particles in the free troposphere over the Taklamakan desert: Electron microscopic experiments of particles collected with a balloonborne particle impactor at Dunhuang, China. *Journal of Geophysical Research*, *108*(D23), 8644. <https://doi.org/10.1029/2002JD003270>
- Jeong, G. Y. (2008). Bulk and single-particle mineralogy of Asian dust and a comparison with its source soils. *Journal of Geophysical Research*, *113*, D02208. <https://doi.org/10.1029/2007JD008606>
- Jeong, G. Y., & Chun, Y. S. (2006). Nanofiber calcite in Asian dust and its atmospheric roles. *Geophysical Research Letters*, *33*, L24802. <https://doi.org/10.1029/2006GL028280>
- Jeong, G. Y., & Nousiainen, T. (2014). TEM analysis of the internal structures and mineralogy of Asian dust particles and the implications for optical modeling. *Atmospheric Chemistry and Physics*, *14*(14), 7233–7254. <https://doi.org/10.5194/acp-14-7233-2014>
- Kim, D. H., Sohn, B. J., Nakajima, T., Takamura, T., Takemura, T., Choi, B. C., & Yoon, S. C. (2004). Aerosol optical properties over east Asia determined from ground-based sky radiation measurements. *Journal of Geophysical Research*, *109*, D02209. <https://doi.org/10.1029/2003JD003387>
- Korean Meteorological Administration (2011). *Asian dust—Time series*. Korean Meteorological Administration: Seoul, Republic of Korea.
- Krueger, B. J., Grassian, V. H., Cowin, J. P., & Laskin, A. (2004). Heterogeneous chemistry of individual mineral dust particles from different dust source regions: The importance of particle mineralogy. *Atmospheric Environment*, *38*(36), 6253–6261. <https://doi.org/10.1016/j.atmosenv.2004.07.010>
- Lafon, S., Rajot, J. L., Alfaro, S. C., & Gaudichet, A. (2004). Quantification of iron oxides in desert aerosol. *Atmospheric Environment*, *38*(8), 1211–1218. <https://doi.org/10.1016/j.atmosenv.2003.11.006>
- Lafon, S., Sokolik, I. N., Rajot, J. L., Caquineau, S., & Gaudichet, A. (2006). Characterization of iron oxides in mineral dust aerosols: Implications for light absorption. *Journal of Geophysical Research*, *111*, D21207. <https://doi.org/10.1029/2005JD007016>
- Lee, K. H., Li, Z. Q., Wong, M. S., Xin, J. Y., Wang, Y. S., Hao, W. M., & Zhao, F. S. (2007). Aerosol single scattering albedo estimated across China from a combination of ground and satellite measurements. *Journal of Geophysical Research*, *112*, D22S15. <https://doi.org/10.1029/2007JD009077>
- Leinen, M., Prospero, J. M., Arnold, E., & Blank, M. (1994). Mineralogy of aeolian dust reaching the North Pacific Ocean. 1. Sampling and analysis. *Journal of Geophysical Research*, *99*(D10), 21,017–21,023. <https://doi.org/10.1029/94JD01735>
- Li, G., Chen, J., Chen, Y., Yang, J., Ji, J., & Liu, L. (2007). Dolomite as a tracer for the source regions of Asian dust. *Journal of Geophysical Research*, *112*, D17201. <https://doi.org/10.1029/2007JD008676>
- Liu, J. J., Zheng, Y. F., Li, Z. Q., Flynn, C., Welton, E. J., & Cribb, M. (2011). Transport, vertical structure and radiative properties of dust events in southeast China determined from ground and space sensors. *Atmospheric Environment*, *45*(35), 6469–6480. <https://doi.org/10.1016/j.atmosenv.2011.04.031>
- Mendonça, B. G. (1969). Local wind circulation on the slopes of Mauna Loa. *Journal of Applied Meteorology*, *8*(4), 533–541. [https://doi.org/10.1175/1520-0450\(1969\)008<0533:lwcofs>2.0.co;2](https://doi.org/10.1175/1520-0450(1969)008<0533:lwcofs>2.0.co;2)
- Merrill, J., Arnold, E., Leinen, M., & Weaver, C. (1994). Mineralogy of aeolian dust reaching the North Pacific Ocean. 2. Relationship of mineral assemblages to atmospheric transport patterns. *Journal of Geophysical Research*, *99*(D10), 21,025–21,032. <https://doi.org/10.1029/94JD01734>
- Okada, K., & Kai, K. (2004). Atmospheric mineral particles collected at Qira in the Taklamakan desert, China. *Atmospheric Environment*, *38*(40), 6927–6935. <https://doi.org/10.1016/j.atmosenv.2004.03.078>

- Okada, K., & Kai, K. J. (1995). Features and elemental composition of mineral particles collected in Zhangye, China. *Journal of the Meteorological Society of Japan*, 73(5), 947–957. https://doi.org/10.2151/jmsj1965.73.5_947
- Park, K., Kittelson, D. B., Zachariah, M. R., & McMurry, P. H. (2004). Measurement of inherent material density of nanoparticle agglomerates. *Journal of Nanoparticle Research*, 6(2/3), 267–272. <https://doi.org/10.1023/B:NANO.0000034657.71309.e6>
- Parrington, J. R., Zoller, W. H., & Aras, N. K. (1983). Asian dust: Seasonal transport to the Hawaiian Islands. *Science*, 220(4593), 195–197. <https://doi.org/10.1126/science.220.4593.195>
- Pye, K. (1987). *Aeolian dust and dust deposits*. London: Harcourt Brace Jovanovich.
- Shaw, G. E. (1980). Transport of Asian desert aerosol to the Hawaiian Islands. *Journal of Applied Meteorology*, 19(11), 1254–1259. [https://doi.org/10.1175/1520-0450\(1980\)019<1254:toadat>2.0.co;2](https://doi.org/10.1175/1520-0450(1980)019<1254:toadat>2.0.co;2)
- Shi, Z. B., Shao, L. T., Jones, T. P., & Lu, S. L. (2005). Microscopy and mineralogy of airborne particles collected during severe dust storm episodes in Beijing, China. *Journal of Geophysical Research*, 110, D01303. <https://doi.org/10.1029/2004JD005073>
- Sokolik, I. N., & Toon, O. B. (1999). Incorporation of mineralogical composition into models of the radiative properties of mineral aerosol from UV to IR wavelengths. *Journal of Geophysical Research*, 104(D8), 9423–9444. <https://doi.org/10.1029/1998JD200048>
- Stein, A. F., Draxler, R. R., Rolph, G. D., Stunder, B. J. B., Cohen, M. D., & Ngan, F. (2015). NOAA'S HYSPLIT atmospheric transport and dispersion modeling system. *Bulletin of the American Meteorological Society*, 96(12), 2059–2077. <https://doi.org/10.1175/bams-d-14-00110.1>
- Su, L., & Toon, O. B. (2011). Saharan and Asian dust: Similarities and differences determined by CALIPSO, AERONET, and a coupled climate-aerosol microphysical model. *Atmospheric Chemistry and Physics*, 11(7), 3263–3280. <https://doi.org/10.5194/acp-11-3263-2011>
- Sullivan, R. C., Guazzotti, S. A., Sodeman, D. A., & Prather, K. A. (2007). Direct observations of the atmospheric processing of Asian mineral dust. *Atmospheric Chemistry and Physics*, 7(5), 1213–1236. <https://doi.org/10.5194/acp-7-1213-2007>
- Svensson, A., Biscaye, P. E., & Grousset, F. E. (2000). Characterization of late glacial continental dust in the Greenland Ice Core Project ice core. *Journal of Geophysical Research-Atmospheres*, 105(D4), 4637–4656. <https://doi.org/10.1029/1999JD901093>
- Tegen, I., & Schepanski, K. (2009). The global distribution of mineral dust. *IOP Conference Series: Earth and Environmental Science*, 7. <https://doi.org/10.1088/1755-1307/7/1/012001>
- Uematsu, M., Duce, R. A., Prospero, J. M., Chen, L., Merrill, J. T., & McDonald, R. L. (1983). Transport of mineral aerosol from Asia over the North Pacific Ocean. *Journal of Geophysical Research*, 88(NC9), 5343–5352. <https://doi.org/10.1029/JC088iC09p05343>
- Uno, I., Eguchi, K., Yumimoto, K., Takemura, T., Shimizu, A., Uematsu, M., et al. (2009). Asian dust transported one full circuit around the globe. *Nature Geoscience*, 2(8), 557–560. <https://doi.org/10.1038/ngeo583>
- Xuan, J., Sokolik, I. N., Hao, J., Guo, F., Mao, H., & Yang, G. (2004). Identification and characterization of sources of atmospheric mineral dust in East Asia. *Atmospheric Environment*, 38(36), 6239–6252. <https://doi.org/10.1016/j.atmosenv.2004.06.042>
- Zhang, X. L., Wu, G. J., Zhang, C. L., Xu, T. L., & Zhou, Q. Q. (2015). What is the real role of iron oxides in the optical properties of dust aerosols? *Atmospheric Chemistry and Physics*, 15(21), 12,159–12,177. <https://doi.org/10.5194/acp-15-12159-2015>
- Zhang, X. Y., Gong, S., Zhao, T., Arimoto, R., Wang, Y., & Zhou, Z. (2003). Sources of Asian dust and role of climate change versus desertification in Asian dust emission. *Geophysical Research Letters*, 30(24), 2272. <https://doi.org/10.1029/2003GL018206>
- Zhou, M., Okada, K., Qian, F., Wu, P.-M., Su, L., Casareto, B. E., & Shimohara, T. (1996). Characteristics of dust-storm particles and their long-range transport from China to Japan—Case studies in April 1993. *Atmospheric Research*, 40(1), 19–31. [https://doi.org/10.1016/0169-8095\(95\)00023-2](https://doi.org/10.1016/0169-8095(95)00023-2)